

Spectral Fingerprints of Earth-like Planets around FGK Stars

S. Rugheimer¹, L. Kaltenegger^{1,2}, A. Zsom^{2,3}, A. Segura⁴, and D. Sasselo¹

Received _____; accepted _____

¹Harvard Smithsonian Center for Astrophysics, 60 Garden st., 02138 MA Cambridge, USA

²MPIA, Koenigstuhl 17, 69117 Heidelberg, Germany

³Department of Earth, Atmospheric and Planetary Sciences, Massachusetts Institute of Technology, Cambridge, MA 02139

⁴Instituto de Ciencias Nucleares, Universidad Nacional Autónoma de México, México

ABSTRACT

We present model atmospheres for an Earth-like planet orbiting the entire grid of main sequence FGK stars with effective temperatures ranging from $T_{\text{eff}} = 4250\text{K}$ to $T_{\text{eff}} = 7000\text{K}$ in 250K intervals. We model the remotely detectable spectra of Earth-like planets for clear and cloudy atmospheres at the 1AU equivalent distance from the VIS to IR ($0.4\ \mu\text{m}$ - $20\ \mu\text{m}$) to compare detectability of features in different wavelength ranges in accordance with JWST and future design concepts to characterize exo-Earths. We also explore the effect of the stellar UV levels as well as spectral energy distribution on a terrestrial atmosphere concentrating on detectable atmospheric features that indicate habitability on Earth, namely: H_2O , O_3 , CH_4 , N_2O and CH_3Cl .

Increased UV dominates changes of O_3 , OH , CH_4 , N_2O and CH_3Cl whereas the increase in stellar temperature dominates changes in H_2O . The overall effect as stellar effective temperatures and corresponding UV increase, is a lower surface temperature of the planet due to a bigger part of the stellar flux being reflected at short wavelengths, as well as increased photolysis. Earth-like atmospheric models show more O_3 and OH but less stratospheric CH_4 , N_2O , CH_3Cl and tropospheric H_2O (but more stratospheric H_2O) with increasing effective temperature of Main Sequence stars. The corresponding spectral features on the other hand show different detectability depending on the wavelength observed.

We concentrate on directly imaged planets here as framework to interpret future lightcurves, direct imaging and secondary eclipse measurements of atmospheres of terrestrial planets in the HZ at varying orbital positions.

Subject headings: Habitability: Planetary Atmospheres: Extrasolar Terrestrial Planets: Spectroscopic Biosignatures

1. INTRODUCTION

Over 830 extrasolar planets have been found to date with thousands more candidate planets awaiting confirmation from NASA’s Kepler Mission. Several of these planets have been found in or near the circumstellar Habitable Zone (see e.g. Batalha et al. 2013; Borucki et al. 2011; Udry et al. 2007; Kaltenegger & Sasselov 2011) with masses and radii consistent with rocky planet models. Recent radial velocity results as well as Kepler demonstrate that small planets in the Habitable Zone (HZ) exist around solar type stars. Future mission concepts to characterize Earth-like planets are designed to take spectra of extrasolar planets with the ultimate goal of remotely detecting atmospheric signatures (e.g. Beichman et al. 1999, 2006; Cash 2006; Traub et al. 2006). For transiting terrestrial planets around the closest stars, the James Web Space Telescope (JWST, see Gardner et al. 2006) as well as future ground and space based telescopes might be able to detect biosignatures by adding multiple transits for the closest stars (see discussion).

Several groups have explored the effect of stellar spectral types on the atmospheric composition of Earth-like planets by considering specific stars: F9V and K2V (Selsis 2000), F2V and K2V (Segura et al. 2003; Grenfell et al. 2007; Kitzmann et al. 2011a,b). In this paper we expand on this work by establishing planetary atmosphere models for the full FGK main sequence, using a stellar temperature grid from 7000K to 4250K, in increments of 250K, to explore the effect of the stellar types on terrestrial atmosphere models. We show the effects of stellar UV and stellar temperature on the planet’s atmosphere individually to understand the overall effect of the stellar type on the remotely detectable planetary spectrum from 0.4-20 μm for clear and cloudy atmosphere models.. This stellar temperature grid covers the full FGK spectral range and corresponds roughly to F0V, F2V, F5V, F7V, F9V/G0V, G2V, G8V, K0V, K2V, K4V, K5V and K7V main sequence stars (following the spectral type classification by Gray 1992).

In this paper we use “Earth-like”, as applied to our models, to mean using modern Earths outgassing rates (following Segura et al. 2003). We explore the influence of stellar spectral energy distribution (SED) on the chemical abundance and planetary atmospheric spectral features for Earth-like planets including biosignatures and their observability from the VIS to IR. Atmospheric biosignatures are chemical species in the atmosphere that are out of chemical equilibrium or are byproducts of life processes. In our analysis we focus particularly on spectral features of chemical species that indicate habitability for a temperate rocky planet like Earth, H_2O , O_3 , CH_4 , N_2O and CH_3Cl (Lovelock 1975; Sagan et al. 1993).

In Section 1 we introduce the photochemistry of an Earth-like atmosphere. In Section 2, we describe our model for calculating the stellar spectra, atmospheric models, and planetary spectra. Section 3 presents the influence of stellar types on the abundance of various atmospheric chemical species. In Section 4 we examine the remote observability of such spectral features, and in Sections 5 and 6 we conclude by summarizing the results and discussing their implications.

1.1. Photochemistry for Earth-like planets including potential biosignatures

For an Earth-like biosphere, the main detectable atmospheric chemical signatures that in combination could indicate habitability are O_2/O_3 with $\text{CH}_4/\text{N}_2\text{O}$, and CH_3Cl . Note that one spectral feature e.g. O_2 does not constitute a biosignature by itself as the planetary context (like bulk planet, atmospheric composition and planet insolation) must be taken into account to interpret this signature. Detecting high concentrations of a reducing gas concurrently with O_2 or O_3 can be used as a biosignature since reduced gases and oxygen react rapidly with each other. Both being present in significant and therefore detectable amounts in low resolution spectra implies a strong source of both. In the IR, O_3 can be

used as a proxy for oxygen at 10^{-2} Present Atmospheric Level of O_2 , the depth of the $9.6 \mu\text{m}$ O_3 feature is comparable to the modern atmospheric level (Kasting et al. 1985; Segura et al. 2003). At the same time, because of the $9.6 \mu\text{m}$ O_3 feature’s non-linear dependence on the O_2 concentration, observing in the visible at $0.76 \mu\text{m}$ would be a more accurate O_2 level indicator, but requires higher resolution than detecting O_3 .

N_2O and CH_3Cl are both primarily produced by life on Earth with no strong abiotic sources, however, their spectral features are likely too small to detect in low resolution with the first generation of missions. While H_2O or CO_2 are not considered biosignatures as both are produced through abiotic processes, they are important indicators of habitability as raw materials and can indicate the level of greenhouse effect on a planet. We refer the reader to other work (e.g. Des Marais et al. 2002; Meadows 2005; Kaltenegger et al. 2010) for a more in depth discussion on habitability and biosignatures. In this section we briefly discuss the most important photochemical reactions involving: H_2O , O_2 , O_3 , CH_4 , N_2O , and CH_3Cl .

Water, H_2O : Water vapor is an important greenhouse gas in Earth’s atmosphere. Over 99% of H_2O vapor is currently in the troposphere, where it is an important source of OH via the following set of reactions:

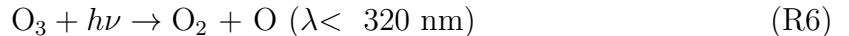
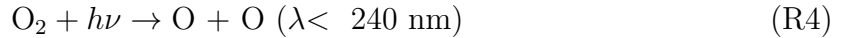


In the troposphere, the production of $O(^1D)$ takes place for $3000 \text{ \AA} < \lambda < 3200 \text{ \AA}$, the lower limit of which is set by the inability of wavelengths, λ shorter than 3000 \AA to reach the troposphere due to O_3 shielding. H_2O , while photochemically inert in the troposphere, can be removed by photolysis primarily by wavelengths shortward of 2000 \AA in the stratosphere. The photodissociation threshold energy is 2398 \AA , but the cross-section

of the molecule above 2000 Å is very low. Stratospheric H₂O can be transported from the troposphere or be formed in the stratosphere by CH₄ and OH.



Oxygen and Ozone, O₂ and O₃: In an atmosphere containing O₂, O₃ concentrations are determined by the absorption of ultraviolet (UV) light shortward of 2400 Å in the stratosphere. O₃ is an oxidizing agent more reactive than O₂, the most stable form of oxygen, due to the third oxygen atom being loosely bound by a single bond. O₃ is also an indirect measure of OH since reactions involving O₃ and H₂O are sources of OH. OH is very reactive and is the main sink for reducing species such as CH₄. O₃ is formed primarily by the Chapman reactions (1930) of the photolysis of O₂ by UV photons (1850 Å < λ < 2420 Å) and then the combining of O₂ with O.



where M is any background molecule such as O₂ or N₂. Reactions [R5] and [R6] are relatively fast compared with [R4] and [R7] which are the limiting reactions in Earth's atmosphere. However, considering the Chapman mechanism alone would overpredict the concentration of O₃ by a factor of two on Earth. Hydrogen oxide (HOx), nitrogen oxide (NOx), and chlorine (ClOx) radicals are the additional sinks controlling the O₃ abundance (Bates & Nicolet, 1950; Crutzen, 1970; Molina and Rowland, 1974, respectively), with NOx and HOx being the dominant and second-most dominant sink, respectively.

Methane, CH₄: Since CH₄ is a reducing gas, it reacts with oxidizing species and thus has a short lifetime of around 10⁻¹² years in modern Earth’s atmosphere (Houghton et al. 2004). In both the troposphere and stratosphere, CH₄ is oxidized by OH, which is the largest sink of the global methane budget. In the stratosphere, CH₄ is also destroyed by UV radiation. Though its photodissociation energy is 2722 Å, its absorption cross-section isn’t sufficient for $\lambda > 1500$ Å. CH₄ is produced biotically by methanogens and termites, and abiotically through hydrothermal vent systems. In the modern atmosphere there is a significant anthropogenic source of CH₄ from natural gas, livestock, and rice paddies. CH₄ is 25x more effective as a greenhouse gas than CO₂ in modern Earth’s atmosphere (Forster et al. 2007) and may have been much more abundant in the early Earth (see e.g. Pavlov et al. 2003).

Nitrous Oxide, N₂O: Nitrous oxide, N₂O, is a relatively minor constituent of the modern atmosphere at around 320 ppbv, with a pre-industrial concentration of 270 ppbv (Forster et al. 2007). It is important for stratospheric chemistry since around 5% is converted to NO, an important sink of O₃, and 95% produces N₂.



On current Earth, N₂O is emitted primarily by denitrifying bacteria with anthropogenic sources from fertilizers in agriculture, biomass burning, industry and livestock.

Methyl Chloride, CH₃Cl: CH₃Cl has been proposed as a potential biosignature because its primary sources are marine organisms, reactions of sea foam and light, and biomass burning (Segura et al. 2005). The primary loss of CH₃Cl in Earth’s atmosphere is by OH as seen in [R9], but it can also be photolyzed or react with atomic chlorine. Because CH₃Cl is a source of chlorine in the stratosphere, it also plays a role in the removal of O₃ as discussed

earlier.



2. MODEL DESCRIPTION

We use EXO-P (Kaltenegger & Sasselov 2010) a coupled one-dimensional radiative-convective atmosphere code developed for rocky exoplanets based on a 1D climate (Kasting & Ackerman 1986; Pavlov et al. 2000; Haqq-Misra et al. 2008), 1D photochemistry (Pavlov & Kasting 2002; Segura et al. 2005, 2007) and 1D radiative transfer model (Traub & Stier 1976; Kaltenegger & Traub 2009) to calculate the model spectrum of an Earth-like exoplanet.

2.1. Planetary Atmosphere Model

EXO-P is a model that simulates both the effects of stellar radiation on a planetary environment and the planet’s outgoing spectrum. The altitude range extends to 60km with 100 layers. We use a geometrical model in which the average 1D global atmospheric model profile is generated using a plane parallel atmosphere, treating the planet as a Lambertian sphere, and setting the stellar zenith angle to 60 degrees to represent the average incoming stellar flux on the dayside of the planet (see also Schindler & Kasting 2000). The temperature in each layer is calculated from the difference between the incoming and outgoing flux and the heat capacity of the atmosphere in each layer. If the lapse rate of

a given layer is larger than the adiabatic lapse rate, it is adjusted to the adiabat until the atmosphere reaches equilibrium. A two-stream approximation (see Toon et al. 1989), which includes multiple scattering by atmospheric gases, is used in the visible/near IR to calculate the shortwave fluxes. Four-term, correlated-k coefficients parameterize the absorption by O_3 , H_2O , O_2 , and CH_4 in wavelength intervals shown in Fig. 1 (Pavlov et al. 2000). In the thermal IR region, a rapid radiative transfer model (RRTM) calculates the longwave fluxes. Clouds are not explicitly calculated. The effects of clouds on the temperature/pressure profile are included by adjusting the surface albedo of the Earth-Sun system to have a surface temperature of 288K (see Kasting et al. 1984; Pavlov et al. 2000; Segura et al. 2003, 2005). The photochemistry code, originally developed by Kasting et al. (1985) solves for 55 chemical species linked by 220 reactions using a reverse-Euler method (see Segura et al. 2010, and references therein).

The radiative transfer model used to compute planetary spectra is based on a model originally developed for trace gas retrieval in Earth’s atmospheric spectra (Traub & Stier 1976) and further developed for exoplanet transmission and emergent spectra (Kaltenegger et al. 2007; Kaltenegger & Traub 2009; Kaltenegger 2010; Kaltenegger et al. 2010). In this paper we model Earth’s reflected and thermal emission spectra using 21 of the most spectroscopically significant molecules (H_2O , O_3 , O_2 , CH_4 , CO_2 , OH , CH_3Cl , NO_2 , N_2O , HNO_3 , CO , H_2S , SO_2 , H_2O_2 , NO , ClO , HOCl , HO_2 , H_2CO , N_2O_5 , and HCl).

Using 34 layers the spectrum is calculated at high spectral resolution, with several points per line width, where the line shapes and widths are computed using Doppler and pressure broadening on a line-by-line basis, for each layer in the model atmosphere. The overall high-resolution spectrum is calculated with 0.1 cm^{-1} wavenumber steps. The figures are shown smoothed to a resolving power of 250 in the IR and 800 in the VIS using a triangular smoothing kernel. The spectra may further be binned corresponding to proposed

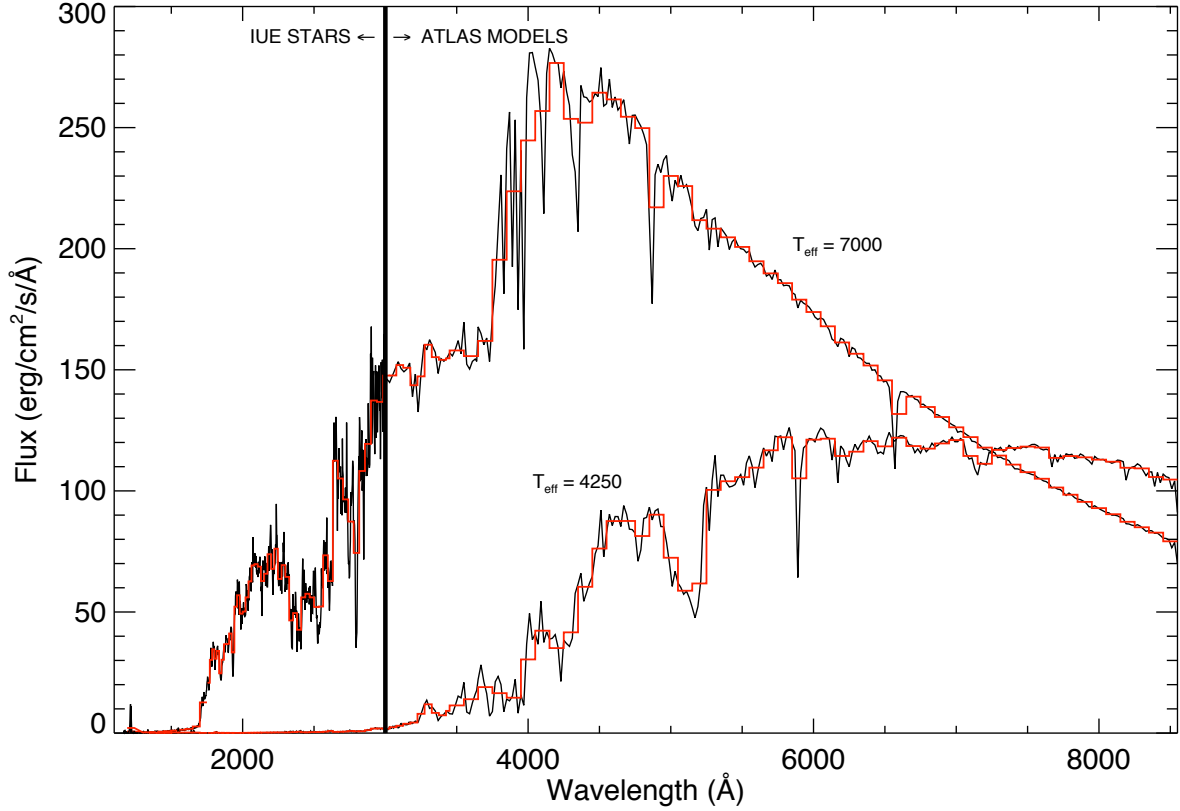


Fig. 1.— F0V and K7V composite input stellar spectrum of IUE observations coadded to (black) ATLAS photospheric models (Kurucz, 1979) and (red) binned stellar input. Note: the full input spectrum extends to 45450 Å. Only the hottest and coolest star in our grid are shown here for comparison.

future spectroscopy missions designs to characterize Earth-like planets.

2.2. Model Validation with EPOXI

We previously validated EXO-P from the VIS to the infrared using data from ground and space (Kaltenegger et al. 2007). Here we use new data by EPOXI in the visible and near-infrared (Livengood et al. 2011) for further validation (see Fig. 2). The data set we use to validate our visible and the near-infrared Earth model spectra is the first EPOXI

observation of Earth which was averaged over 24 hours on 03/18/2008 - 03/19/2008 and taken at a phase angle of 57.7° . The uncertainty in the EPOXI calibration is $\approx 10\%$ (Klaasen et al. 2008). Atmospheric models found the best match to be for a 50% cloud coverage with 1.5km and 8.5km cloud layer respectively (Robinson et al. 2011).

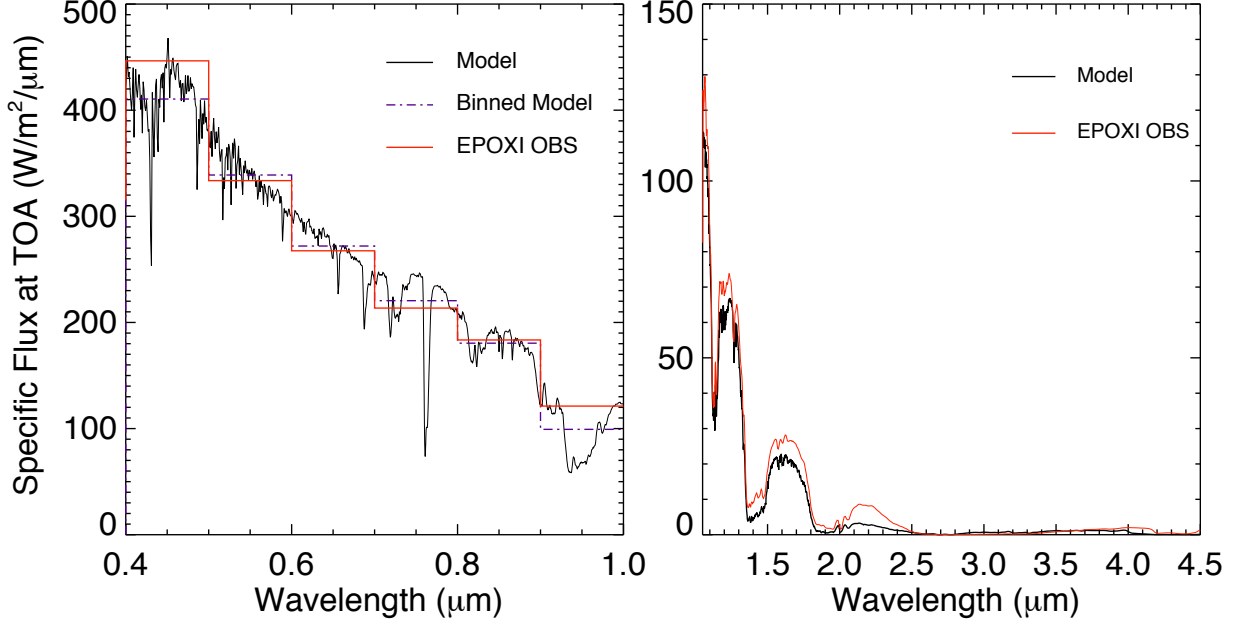


Fig. 2.— Comparison of EPOXI data (red) with the Earth model, top-of-atmosphere spectrum at full phase from EXO-P (black) in the visible (left) and near-infrared (right).

Here we use a 60% global cloud cover spectrum divided between three layers: 40% water clouds at 1km, 40% water clouds at 6km, and 20% ice clouds at 12km (following Kaltenegger et al. 2007) consistent with an averaged Earth profile to compare our model to this 24hr data set, which should introduce slight discrepancies. To correct the brightness values to match to our full-phase model we use a Lambert phase function.

Our model agrees with EPOXI on an absolute scale within 1-3% for the middle photometric points. The largest discrepancies in the visible are at $0.45 \mu\text{m}$ and $0.95 \mu\text{m}$ (with a 8% and 18% error respectively).

2.3. Stellar Spectral Grid Model

The stellar spectra grid ranges from 4250K to 7000K in effective temperature increments of 250K. This temperature range effectively probes the F0 to K7 main sequence spectral types. For each model star on our grid we concatenated a solar metallicity, unreddened synthetic ATLAS spectrum, which only considers photospheric emission (Kurucz 1979), with observations from the International Ultraviolet Explorer (IUE) archive. We use IUE measurements to extend ATLAS synthetic spectra, to generate input spectra files from 1150Å to 45,450Å (see Figs. 1 and 2). We choose main sequence stars in the IUE archive with corresponding temperatures close to the grid temperatures and near solar metallicity, as described below.

The IUE satellite had three main cameras, the longwave (LWP/LWR) cameras (1850Å - 3350Å), and the shortwave (SW) camera (1150Å - 1975Å). When preparing the IUE data (following Segura et al. 2003; Massa & Fitzpatrick 1998, 2000), we used a sigma-weighted average to coadd the multiple SW and LW observations. We used a linear interpolation when there was insufficient high quality measurements to merge the wavelength region from the SW to the LW cameras. IUE measurements were joined to ATLAS model spectra at 3000 Å. In a few cases, a shift factor is needed to match the IUE data to the ATLAS model (Segura et al. 2003, see also) but unless stated explicitly no shift factor was used. Effective temperatures and metallicities are taken from NStED (derived from Flower 1996; Valenti & Fischer 2005, , respectively) unless otherwise cited. See Table 1 for a summary list of the representative IUE stars chosen.

HD 40136, η Lep, is at 15.04pc with a $T_{\text{eff}} = 7060\text{K}$ and $[\text{Fe}/\text{H}] = -0.13$ (de Strobel et al. 2001), corresponding to an F0V, the hottest model grid star. Two LW and four SW spectra were coadded and merged with a 7000K ATLAS spectrum.

To compare with previous work (Segura et al. 2003; ?; Selsis 2000), we chose HD

Table 1: List of representative IUE stars with their measured T_{eff} , the T_{eff} which corresponds to our grid of stars, their metallicity, and their approximate stellar type following Gray (1992).

Star	T_{eff} (K)	T_{eff} (K) Grid	[Fe/H]	Spectral Type Grid
η Lep	7060	7000	-0.13	F0V
σ Boo	6730	6750	-0.43	F2V
π^3 Ori	6450	6500	0.03	F5V
ι Psc	6240	6250	-0.09	F7V
β Com	5960	6000	0.07	F9V/G0V
α Cen A	5770	5750	0.21	G2V
τ Ceti	5500	5500	-0.52	G8V
HD 10780	5260	5250	0.03	K0V
ϵ Eri	5090	5000	-0.03	K2V
ϵ Indi	4730	4750	-0.23	K4V
61 Cyg A	4500	4500	-0.43	K5V
BY Dra	4200	4250	0.00	K7V

128167, σ Boötis, for our model F2V grid star. σ Boötis is an F2V star at 15.47pc with $T_{\text{eff}} = 6730\text{K}$ and $[\text{Fe}/\text{H}] = -0.43$. Two LW and five SW spectra were coadded and merged with a 6750K ATLAS spectrum. A slight downward shift of a factor of 0.88 is necessary to match the IUE data with a ATLAS spectrum (see also Segura et al. 2003).

π^3 Orionis, HD 30652, is at 8.03pc with a $T_{\text{eff}} = 6450\text{K}$ and $[\text{Fe}/\text{H}] = 0.03$, corresponding to an F5V grid star. Two LW and three SW spectra were coadded and merged with a 6500K ATLAS spectrum.

ι Piscium, HD 222368, is at 13.79pc with a $T_{\text{eff}} = 6240\text{K}$ and $[\text{Fe}/\text{H}] = -0.09$, corresponding to an F7V grid star. Two LW and four SW spectra were coadded and merged with a 6250K ATLAS spectrum.

β Com, HD 114710, is at 9.15pc with a $T_{\text{eff}} = 5960\text{K}$ and $[\text{Fe}/\text{H}] = 0.07$, corresponding to an G0V grid star. Only one LW spectrum was correctable with the Massa routines and thus one LW and five SW spectra were coadded and merged with a 6000K ATLAS

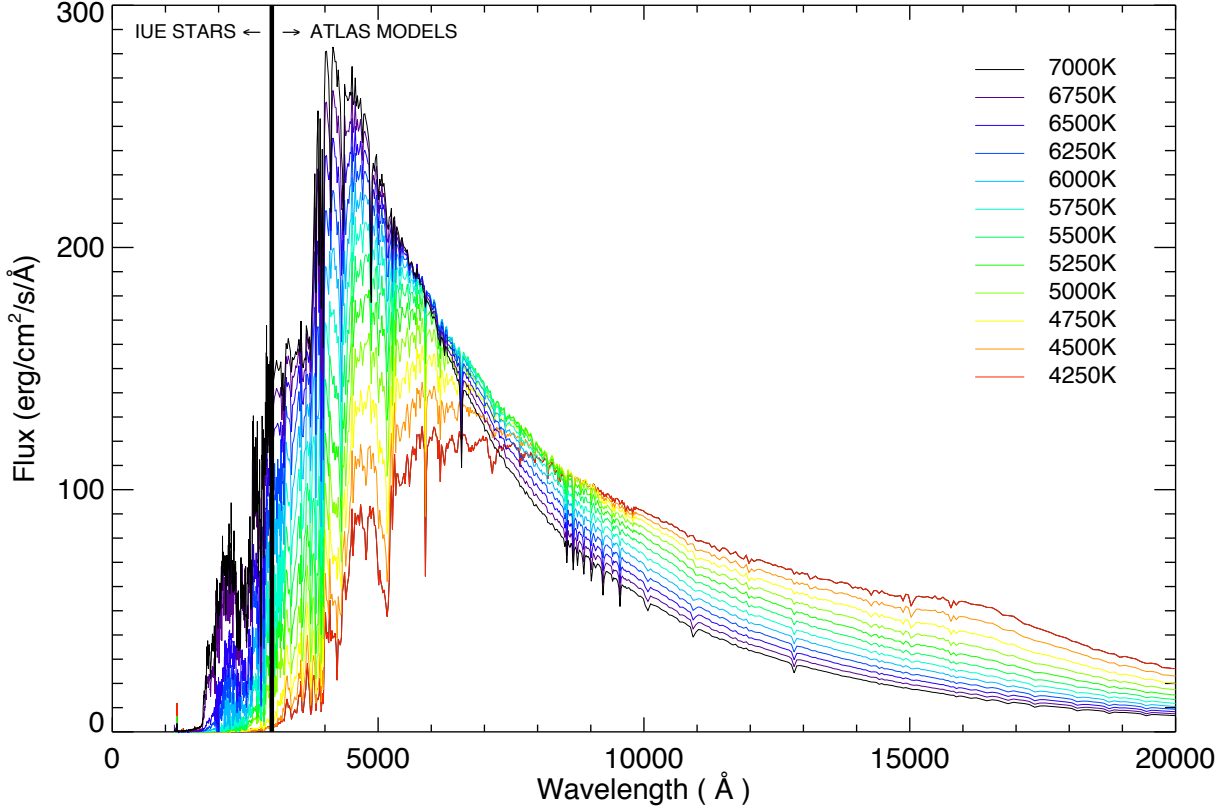


Fig. 3.— Composite stellar input spectra from IUE observations merged to a ATLAS photosphere model at 3000 Å for each grid star. We display up to 20,000 here however the complete input files extend to 45,450 Å.

spectrum.

α Centauri A, HD 128620, is at 1.35 pc with a $T_{\text{eff}} = 5770\text{K}$ and $[\text{Fe}/\text{H}] = 0.21$, corresponding to a G2V grid star. Three LW and 93 SW spectra were coadded and merged with an upward shift of 1.25 to a 5750K ATLAS spectrum.

τ Ceti, HD 10700, is at 3.65pc with $T_{\text{eff}} = 5500\text{K}$ and $[\text{Fe}/\text{H}] = -0.52$, corresponding to a G8V grid star. Two LW and eight SW spectra were coadded and merged with a 5500K ATLAS spectrum.

HD 10780 is at 9.98pc with $T_{\text{eff}} = 5260\text{K}$ and $[\text{Fe}/\text{H}] = 0.03$, corresponding to a K0V grid star. It is a variable of the BY Draconis type. Five LW and four SW spectra were coadded and merged with a 5250K ATLAS spectrum.

ϵ Eridani, HD 22049, is at 3.22pc with $T_{\text{eff}} = 5090\text{K}$ and $[\text{Fe}/\text{H}] = -0.03$, corresponding to a K2V grid star. ϵ Eri was chosen to compare with previous work (Segura et al. 2003; ?; Selsis 2000). ϵ Eri is a young star, only 0.7 Ga (Di Folco et al. 2004), and is thus more active than a typical K-dwarf. Due to its variability and close proximity there are frequent IUE observations. 17 LW and 72 SW IUE spectra were coadded and merged these with a 5000K ATLAS spectrum.

ϵ Indi, HD 209100, is at 3.63 pc with $T_{\text{eff}} = 4730\text{K}$ and $[\text{Fe}/\text{H}] = -0.23$, corresponding to a K4V grid star. Seven LW and 30 SW IUE spectra were coadded and merged with a 4750K ATLAS spectrum.

61 Cyg A, HD 201091, is at 3.48 pc with $T_{\text{eff}} = 4500\text{K}$ and $[\text{Fe}/\text{H}] = -0.43$ (de Strobel et al. 2001), corresponding to a K5V grid star. 61 Cyg A is a variable star of the BY Draconis type. Six LW and twelve SW spectra were coadded and merged with an upward shift of 1.15 to match the 4500K ATLAS spectrum.

BY Dra, HD 234677, is at 16.42pc with a $T_{\text{eff}} = 4200\text{K}$ (Hartmann et al., 1977) and $[\text{Fe}/\text{H}] = 0$ (Cayrel de Strobel et al. 1997), corresponding to a K7V grid star. It is, not surprisingly, a variable of the BY Draconis type. Eight LW and 30 SW spectra were coadded and merged to the 4250K ATLAS spectrum.

All input stellar spectra are shown in Fig. 3.

2.4. Simulation Set-Up

To examine the effect of the SED of the host star on an Earth-like atmosphere, we build a temperature grid of stellar models ranging from 7000K to 4250K in steps of 250K, corresponding to F type stars to K dwarfs. We simulated an Earth-like planet with the same mass as Earth at the 1AU equivalent orbital distance, where the wavelength integrated stellar flux received on top of the planet’s atmosphere is equivalent to 1AU in our solar system, 1370 W/m^{-2} .

The biogenic fluxes were held fixed in the models in accordance with the fluxes that reproduce the modern mixing ratios in the Earth-Sun case (following Segura et al., 2003). We first calculate the surface fluxes for long-lived gases H_2 , CH_4 , N_2O , CO and CH_3Cl . Simulating the Earth around the Sun with 100 layers yields a $T_{\text{surf}} = 288\text{K}$ for surface mixing ratios: $c\text{H}_2 = 5.5 \times 10^{-7}$, $c\text{CH}_4 = 1.6 \times 10^{-6}$, $c\text{CO}_2 = 3.5 \times 10^{-4}$, $c\text{N}_2\text{O} = 3.0 \times 10^{-7}$, $c\text{CO} = 9.0 \times 10^{-8}$, and $c\text{CH}_3\text{Cl} = 5.0 \times 10^{-10}$. The corresponding surface fluxes are $-1.9 \times 10^{12} \text{ g H}_2/\text{year}$, $5.3 \times 10^{14} \text{ g CH}_4/\text{year}$, $7.9 \times 10^{12} \text{ g N}_2\text{O per year}$, $1.8 \times 10^{15} \text{ g CO/year}$, and $4.3 \times 10^{12} \text{ g CH}_3\text{Cl/year}$. The best estimate for the modern CH_4 flux is $5.35 \times 10^{14} \text{ g/year}$ (Houghton et al., 2004) and corresponds to the value derived in the model. Fluxes for the other biogenic species are poorly constrained. The N_2 concentration is set by the total surface pressure of 1 bar. To explore the effect of UV and temperature separately, we combine a certain ATLAS model with varying UV files and vice versa.

3. ATMOSPHERIC MODEL RESULTS AND DISCUSSION

The stellar spectrum has two effects on the atmosphere: first, the UV effect (section 3.1) that primarily influences photochemistry and second, the temperature effect (section 3.2) resulting from the difference in absorbed flux as a function of stellar SED. The

same planet has a higher Bond albedo around hotter stars with SEDs peaking at shorter λ , where Rayleigh scattering is more efficient, than around cooler stars, assuming the same total stellar flux (Sneep & Ubachs 2005). The overall resulting planetary Bond albedo that includes both atmospheric as well as surface albedo is calculated by the climate/photochemistry model and varies between 0.13 - 0.22 for planets around F0 stars to K7 stars respectively because of the stars' SED. Note that these values are lower than Earth's planetary Bond albedo of 0.31 because the warming effect of clouds is folded into the albedo value in the climate code, decreasing it artificially.

3.1. The influence of UV levels on Earth-like atmosphere models (UV effect)

To explore the effects of UV flux alone on the atmospheric abundance of different molecules, we combined specific IUE data files for stars with $T_{\text{eff}} = 7000\text{K}$, 6000K and 4500K (representing high, mid and low UV flux) with a fixed ATLAS photospheric models of $T_{\text{eff}} = 6000\text{K}$. The temperature/pressure and chemical profiles of this test are shown in panels a) of Figs. 4 and 5. Hot stars provide high UV flux in the 2000 - 3200 Å range, e.g. a F0V grid star emits 130x more flux in this wavelength range than a K7V grid star (Figs. 1 and 2).

The Chapman reactions are driven primarily by photolysis in this wavelength range and the atmosphere models show an according increase in O_3 concentration and subsequent strong temperature inversion for planets orbiting hot grid stars (Table 2). The maximum heating in the stratosphere is a few kilometers above the peak of the O_3 concentration where both a high enough concentration of O_3 and a high enough flux of photons is present. O_3 abundance increases OH abundance, the primary sink of CH_4 and CH_3Cl . Figs. 5 and 7 shows a corresponding decrease in those molecules for high UV environment. O_3 shields H_2O in the troposphere from UV environments. Stratospheric H_2O is photolyzed

Table 2: Surface temperature and O₃ column depth for an Earth-like planet model orbiting the grid stars.

$T_{\text{eff}}(\text{K})$ Grid	Spectral Type Grid	Surface Temp (K)	Ozone Column Depth (cm^{-2})
7000	F0V	279.9	1.210^{19}
6750	F2V	281.7	1.110^{19}
6500	F5V	283.2	9.610^{18}
6250	F7V	284.6	8.310^{18}
6000	F9V/G0V	286.4	7.310^{18}
SUN	G2V	288.1	5.310^{18}
5750	G2V	287.7	5.110^{18}
5500	G8V	289.1	3.210^{18}
5250	K0V	290.9	4.110^{18}
5000	K2V	291.9	3.310^{18}
4750	K4V	292.8	2.610^{18}
4500	K5V	297.0	2.610^{18}
4250	K7V	300.0	3.510^{18}

by $\lambda < 2000 \text{ \AA}$ or reacts with excited oxygen, O1D to produce OH radicals. Accordingly stratospheric H₂O concentration decreases with decreasing UV flux. N₂O decreases with increasing UV flux because of photolysis by $\lambda < 2200 \text{ \AA}$. N₂O is also an indirect sink for stratospheric O₃ when it is converted to NO. Therefore decreasing N₂O increases O₃ abundance. O₂ and CO₂ concentrations remain constant and well mixed for all stellar types.

3.2. The influence of stellar T_{eff} on Earth-like atmosphere models (Temperature effect)

To explore the effects of stellar T_{eff} alone on the atmospheric abundance of different molecules, we combined specific photospheric ATLAS spectrum of $T_{\text{eff}} = 7000\text{K}$, 6000K and 4500K (representing high, mid and low stellar T_{eff}) with a fixed UV data file of $T_{\text{eff}} = 6000\text{K}$. The temperature/pressure and chemical profiles of this test are shown in panels b) of Figs. 4 and 5. T_{eff} affects H₂O vapor concentrations due to increased evaporation for

high planetary surface temperature which is transported to the stratosphere. Fig. 4 shows an overall increase in tropopause and stratopause height for low stellar T_{eff} with according hot planetary surface temperatures.

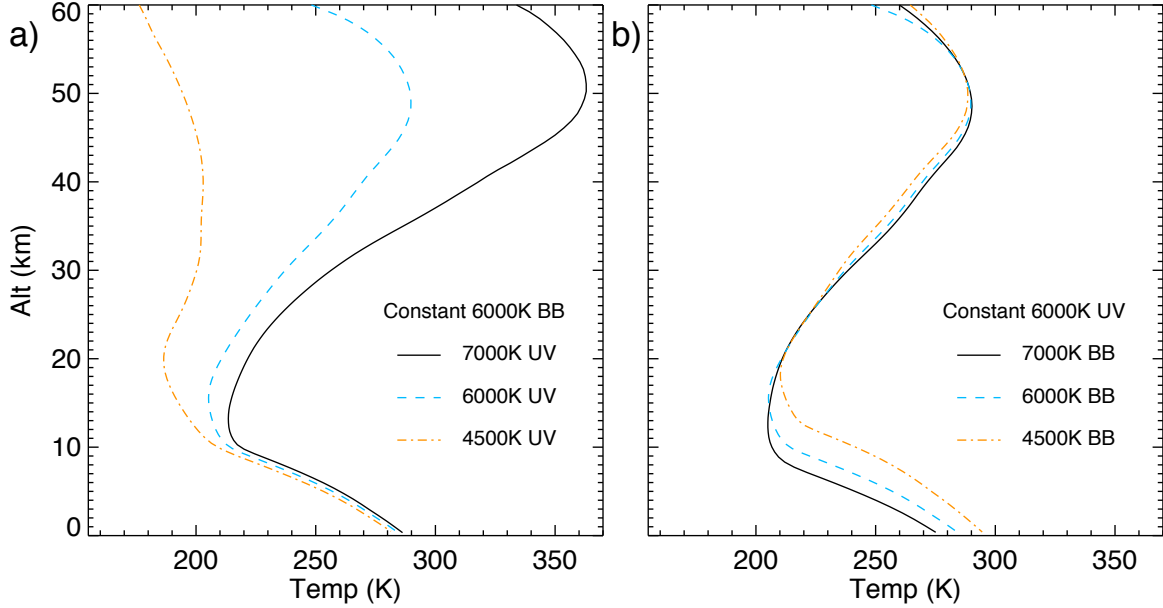


Fig. 4.— Temperature/altitude profiles for several unphysical test where we: a) combine high, mid, and low UV fluxes (IUE observations for stars with $T_{\text{eff}} = 7000\text{K}$, 6000K , and 4500K , respectively) with a fixed ATLAS photosphere model for $T_{\text{eff}} = 6000\text{K}$ to show the “UV effect,” and b) combine high, mid, and low stellar photosphere models (ATLAS models for $T_{\text{eff}} = 7000\text{K}$, 6000K , and 4500K , respectively) with a fixed UV flux for $T_{\text{eff}} = 6000\text{K}$ to show the “Temperature effect.”

The response of O_3 to stellar T_{eff} is weak due to two opposing effects: high stellar T_{eff} and according low planetary surface and atmospheric temperatures increase O_3 concentration by slowing Chapman reactions that destroy O_3 , but also increase NOx , HOx , and ClOx concentrations which are the primary sinks of O_3 (see also Grenfell et al. 2007).

Both CH_4 and CH_3Cl show only a weak temperature dependence. The rate of the

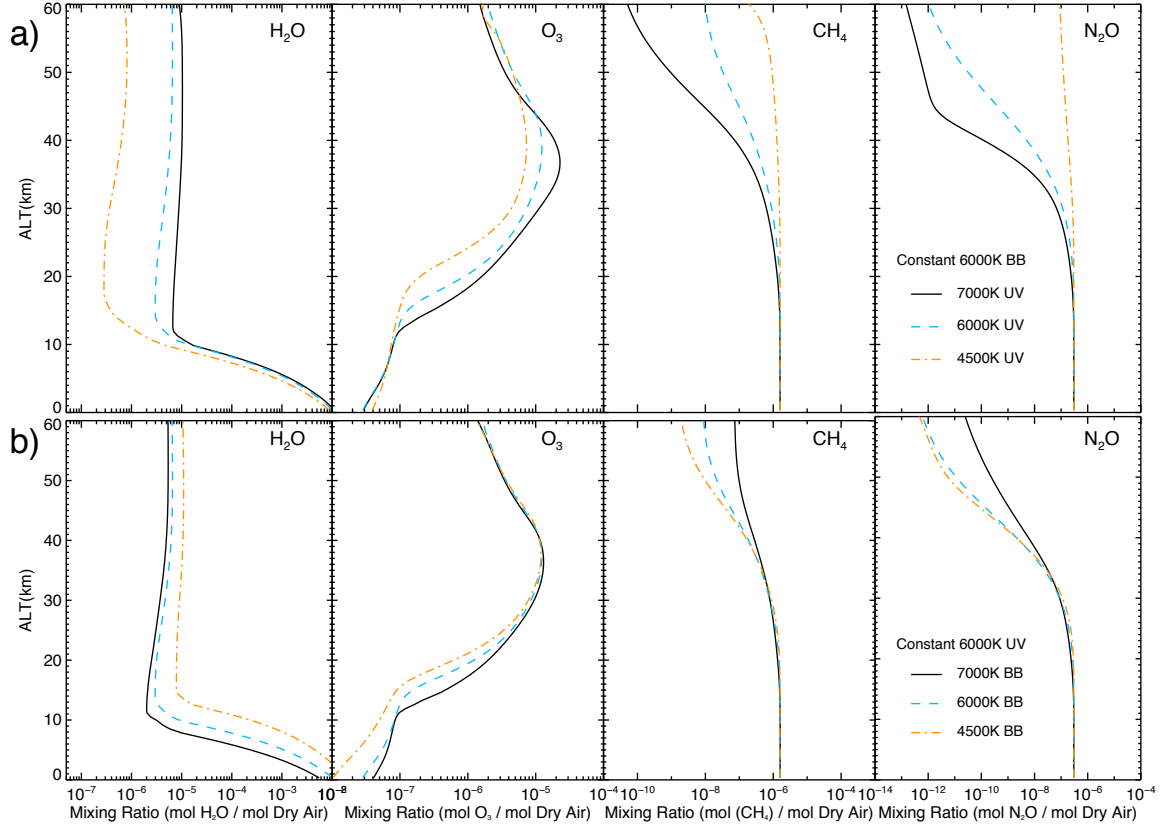


Fig. 5.— Chemical mixing ratio profiles for H_2O , O_3 , CH_4 , and N_2O from several unphysical test where we: a) combine high, mid, and low UV fluxes (IUE observations for stars with $T_{\text{eff}} = 7000\text{K}$, 6000K , and 4500K , respectively) with a fixed ATLAS photosphere model for $T_{\text{eff}} = 6000\text{K}$ to show the “UV effect”, and b) combine high, mid, and low stellar photosphere models (ATLAS models for $T_{\text{eff}} = 7000\text{K}$, 6000K , and 4500K , respectively) with a fixed UV flux for $T_{\text{eff}} = 6000\text{K}$ to show the “Temperature effect.”

primary reactions of CH_4 and CH_3Cl with OH slows with decreasing temperature, causing an increase in CH_4 and CH_3Cl for lower planetary surface temperatures. N_2O displays a similar weak temperature effect. All of our simulations used a fixed mixing ratio of 355ppm for CO_2 and 21% O_2 . Since both O_2 and CO_2 are well mixed in the atmosphere, their vertical mixing ratio profiles are not shown.

3.3. The influence of stellar SED on Earth-like atmosphere models

Figs. 6 and 7 show the combined temperature and UV effect on Earth-like atmospheres. The surface temperature of an Earth-like planet increases with decreasing stellar effective temperature due to decreasing reflected stellar radiation and increasing IR absorption by H_2O and CO_2 (see Table 2 and Fig. 6). The late K-dwarf stars show in addition a near isothermal stratosphere.

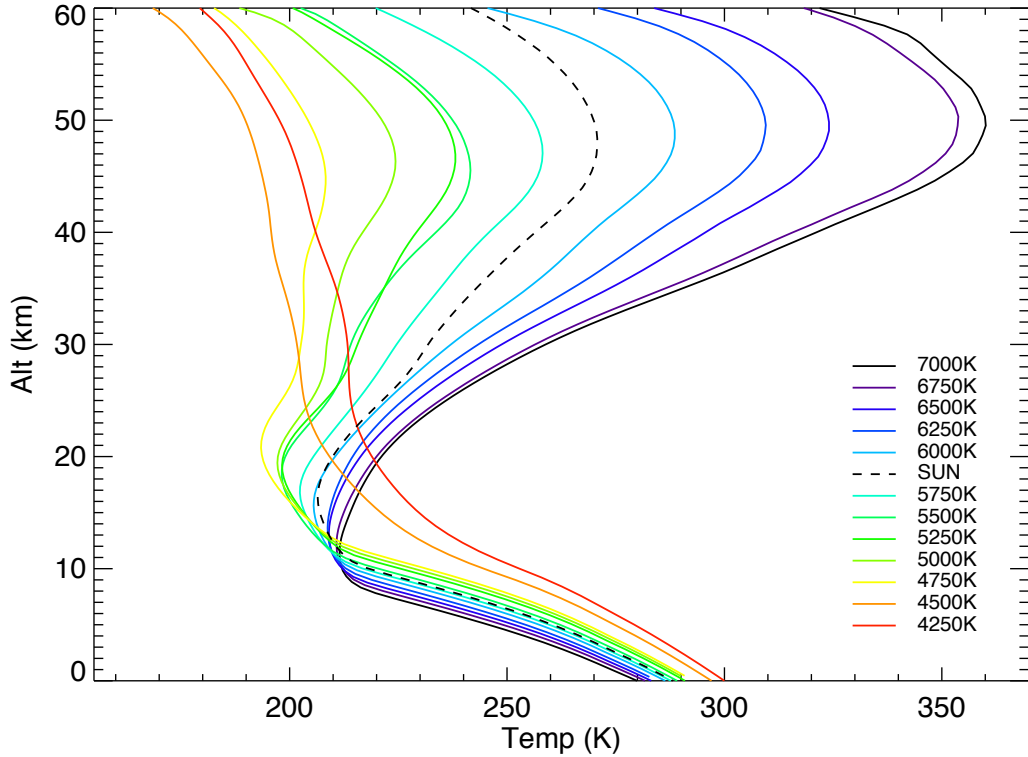


Fig. 6.— Planetary temperature/altitude profiles for different stellar types showing the combined temperature and UV effect.

Fig. 7 shows the corresponding atmospheric mixing ratios versus height for the grid stars. The top height considered in our atmosphere models is 60 km for a Sun-like star, which corresponds to 10^{-4} bar (following Segura et al. 2003). For hotter stars the stratosphere is warmer increasing the pressure at 60 km to 4.0×10^{-4} bars while for cooler

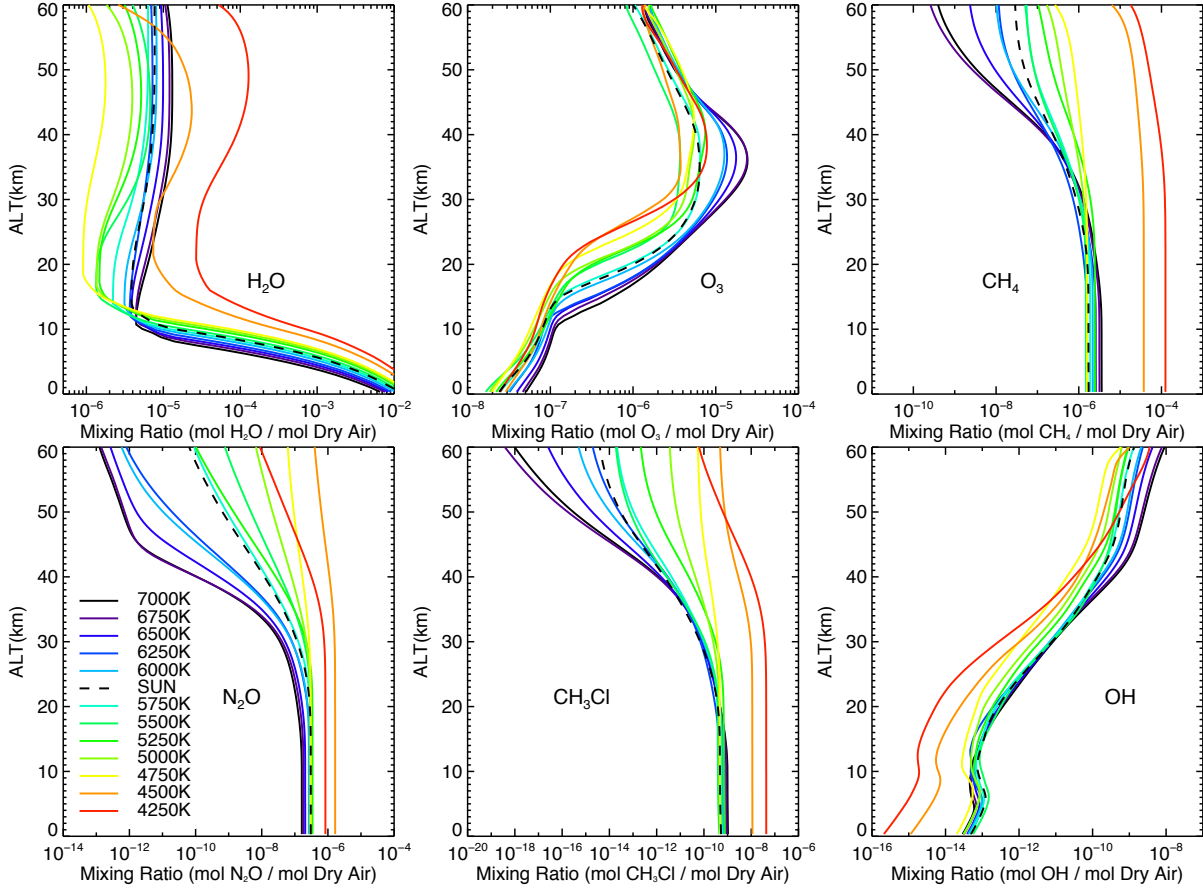


Fig. 7.— Photochemical model results for the mixing ratios of the major molecules H_2O , O_3 , CH_4 , N_2O , CH_3Cl , and OH for each stellar spectral type in our grid of stars showing the combined temperature and UV effect.

stars the pressure at 60 km decreases to 3.0×10^{-5} bars.

Earth-like atmosphere models around hot grid stars show high O_3 concentration (see Table 2) and therefore strong temperature inversions due to the increased stellar UV flux (Fig. 6). Cooler stars often have stronger emission lines and higher activity. Accordingly the coldest two grid stars in our sample ($T_{\text{eff}} = 4250\text{K}$ and 4500K) show a large O_3 abundance due to high stellar Ly- α flux. In fact, the UV output of the coldest grid star,

$T_{\text{eff}} = 4250\text{K}$ is almost 2x the UV flux of the second coldest grid star, $T_{\text{eff}} = 4500\text{K}$, also due to its younger age. Thus, there is more O_3 produced for the coldest star. However, in the 2000 - 3000 Å wavelength region these cold grid stars emit low UV flux and therefore produce near isothermal stratospheres (see also M-dwarf models in Segura et al. 2005). The detailed effect of Ly- α flux on the planet’s atmosphere, will be modeled in a future paper.

Earth-like atmosphere models around hot grid stars also show high OH concentrations due to a higher availability of high energy photons, as well as O_3 and H_2O molecules (Fig. 7). Cold grid stars ($T_{\text{eff}} = 4250\text{K}$) show higher OH concentration in the stratosphere than expected from an extrapolation from the other grid stars due to the increased O_3 and H_2O concentrations at those altitudes.

CH_4 abundance increases with decreasing stellar temperature, dominated by the effects of decreasing stellar UV. Stratospheric CH_4 decreases in atmosphere models around hot grid stars since both OH concentration and UV flux increase with stellar T_{eff} and act as sinks of CH_4 .

H_2O abundance in the troposphere is dominated by the surface temperature of the planet. Earth-like planet atmosphere models around cool grid stars, generate warmer planetary surface temperatures, and therefore high amounts of tropospheric H_2O . High UV flux generally decreases H_2O concentration in the stratosphere through photolysis but increased O_3 concentrations provides shielding from the photolysis of H_2O . Also cold grid stars ($T_{\text{eff}} = 4250\text{K}$ and 4500K) show increased stratosphere H_2O concentration through increased vertical transport in the nearly isothermal stratospheres as well as production by stratospheric CH_4 (see e.g. Segura et al. 2005, for similar behavior in planets around M-dwarfs). In particular, the atmosphere models for a planet around $T_{\text{eff}} = 4250\text{K}$ grid star has a high OH concentration in the stratosphere due to increased O_3 and H_2O at those altitudes.

N_2O is primarily produced by denitrifying bacteria and has increased linearly due to agriculture since the preindustrial era at a rate of around $0.26\% \text{ yr}^{-1}$ (Forster et al. 2007). Up to about 20km, there is no significant difference between stellar types in N_2O concentration. Above 20km, Fig. 7 shows a decrease in N_2O concentration for atmosphere models around hot compared to cool grid stars since UV is the primary sink of N_2O in the stratosphere. Below 20km N_2O is shielded from photolysis by the O_3 layer. Note that the general trend for increasing N_2O for colder grid stars reverses for our coldest grid star. This is due to the increased UV flux which destroys N_2O and an increase in O_3 which causes an increase in $\text{O}(^1\text{D})$, another strong sink for N_2O .

CH_3Cl concentration decreases with increased stellar UV flux since OH which act as sink for CH_3Cl .

4. RESULTS: SPECTRA OF EARTH-LIKE PLANETS ORBITING F0V TO K7V GRID STARS

We include both a clear sky as well as a 60% global cloud cover spectrum which has cloud layers analogous to Earth (40% 1km, 40% 6km and 20% 12km following Kaltenegger et al. (2007)) in Figs. 8-11 to show the importance of clouds on the reflected and emission planet spectra. We present the spectra as specific flux at the top of the atmosphere of Earth-like planets. In the VIS, the depth of the absorption features is primarily sensitive to the abundance of the species, while in the IR, both the abundance and the temperature difference between the emitting/absorbing layer and the continuum influences the depth of features.

We use a Lambert sphere as an approximation for the disk integrated planet in our model. The surface of our model planet corresponds to Earth’s current surface of 70%

ocean, 2% coast, and 28% land. The land surface consists of 30% grass, 30% trees, 9% granite, 9% basalt, 15% snow, and 7% sand. Surface reflectivities are taken from the USGS Digital Spectral Library¹ and the ASTER Spectral Library² (following Kaltenegger et al. 2007). Note the vegetation red edge feature at $0.76 \mu\text{m}$ is only detectable in the clear sky model spectra in low resolution, see Fig. 8 (see e.g. Kaltenegger et al. 2007; Seager et al. 2005; Pallé et al. 2008). No noise has been added to these model spectra to provide input models for a wide variety of instrument simulators for both secondary eclipse and direct detection simulations.

We assume full phase (secondary eclipse) for all spectra presented to show the maximum flux that can be observed. Note that we use an Earth-size planet to determine the specific flux and planet-to-star contrast ratio. A Super-Earth with up to twice Earth’s radius will provide 4 times more flux and a better contrast ratio than shown in Figs. 8 to 14.

4.1. Earth-like Visible/Near-infrared Spectra ($0.4\mu\text{m} - 4\mu\text{m}$)

Fig. 8 shows emergent spectra from 0.4 to $2\mu\text{m}$ of Earth-like planets for both a clear-sky and Earth-analogue cloud cover for the grid stars (F0V-K7V). The high resolution spectra have been smoothed to a resolving power of 800 using a triangular smoothing kernel. Figs. 8 and 9 show that clouds increase the reflectivity of an Earth-like planet in the VIS to NIR substantially and therefore overall increase the equivalent width of all observable feature, even though they block access to some of the lower atmosphere.

Fig. 9 shows individual features for the strongest atmospheric features from 0.4 to

¹<http://speclab.cr.usgs.gov/spectral-lib.html>

²<http://speclib.jpl.nasa.gov>

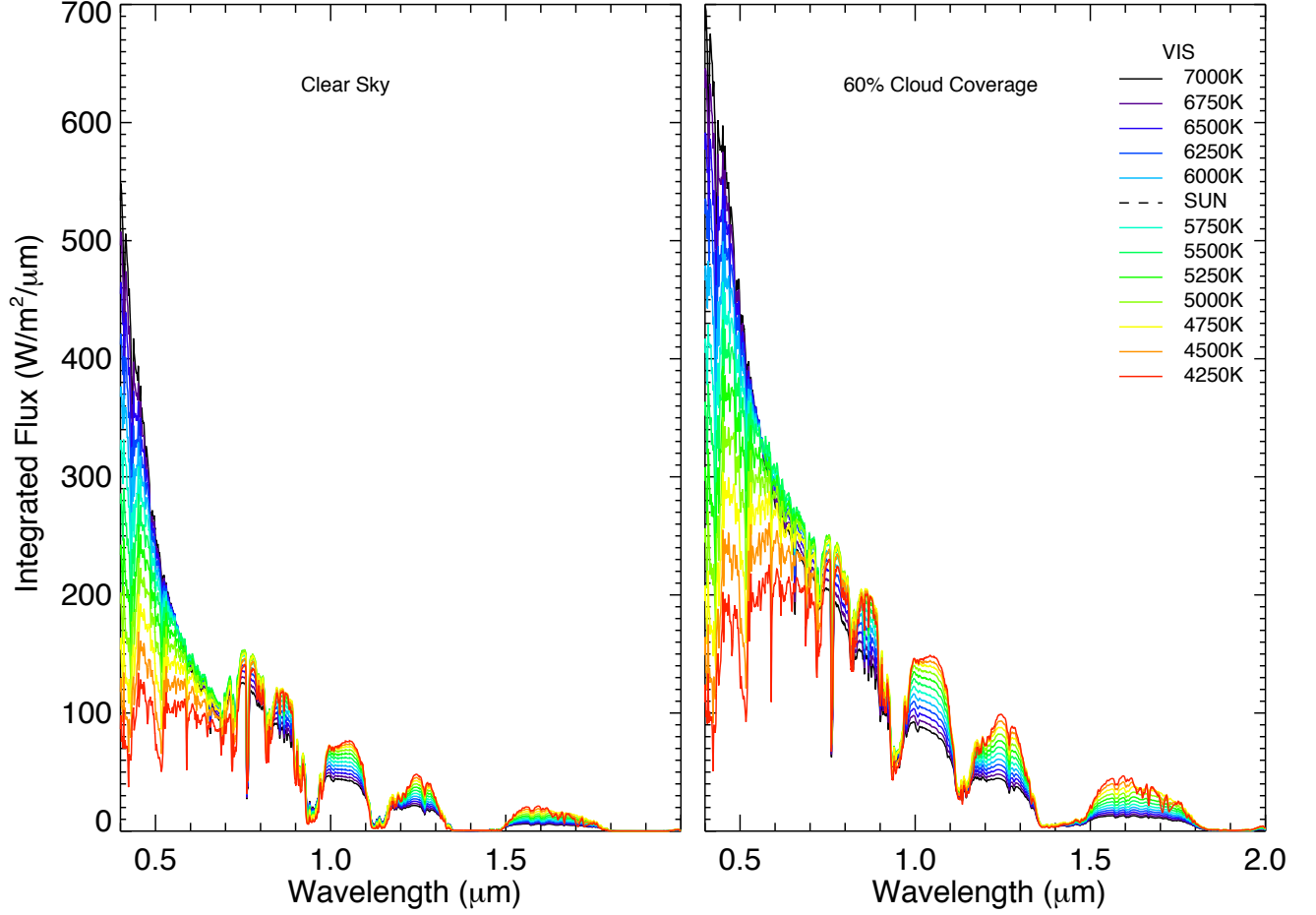


Fig. 8.— Smoothed, disk-integrated VIS/NIR spectra at the top of the atmosphere (TOA) for an Earth-like planet around FGK stars for both a clear sky (left) and 60% cloud coverage (right) model (region 2-4 μm has low integrated flux levels and therefore is not shown here).

4 μm for Earth-like planets orbiting the grid stars: O₃ at 0.6 μm (the Chappuis band), O₂ and 0.76 μm , H₂O at 0.95 μm , and CH₄ at 1.7 μm . The left panel of each row shows the relative flux as planet-to-star contrast ratio, the middle and right panel show the specific, top-of-atmosphere flux for a clear and 60% cloud cover, respectively. From the planet-to-star contrast ratios in Figs. 9, 11 and 13 the photometric precision required

to detect these features for Earth-like planets can be calculated. Note that any shallow spectral features like the visible O_3 feature would require a very high SNR to be detected.

The $0.6 \mu\text{m}$ shallow O_3 spectral feature depth increases with T_{eff} of the star host since O_3 concentration increases with UV levels but is difficult to distinguish from Rayleigh scattering. The relative depth of the O_2 feature at $0.76 \mu\text{m}$ is constant but the flux decreases for cool grid stars due to the decrease in absolute stellar flux received and reflected by the planet at short wavelengths. The depth of the H_2O absorption feature at $0.9 \mu\text{m}$ (shown) 0.8 , 1.1 and $1.4 \mu\text{m}$ increase for planets orbiting cool grid stars due to their increased H_2O abundance. The depth of the CH_4 absorption feature at $1.7 \mu\text{m}$ increases with decreasing stellar T_{eff} due to the increase of CH_4 abundance.

From 2 to $4 \mu\text{m}$ there are CH_4 features at $2.3 \mu\text{m}$ and $3.3 \mu\text{m}$, a CO_2 feature at $2.7 \mu\text{m}$, and H_2O absorption at $2.7 \mu\text{m}$ and $3.7 \mu\text{m}$. However, due to the low emergent flux in this region, these features are not shown individually.

4.2. Earth-like Infrared Spectra, IR ($4 \mu\text{m}$ - $20 \mu\text{m}$)

Fig. 10 shows emergent spectra from 4 to $20 \mu\text{m}$ of Earth-like planets for both a clear sky and Earth-analogue cloud cover for the grid stars (F0V-K7V). The high resolution spectra have been smoothed to a resolving power of 250 using a triangular smoothing kernel. Clouds decrease the overall emitted flux of an Earth-like planet in the IR.

Fig. 11 shows individual features for the strongest atmospheric features from 4 to $20 \mu\text{m}$ for Earth-like planets orbiting the grid stars: O_3 at $9.6 \mu\text{m}$, CO_2 at $15 \mu\text{m}$, H_2O at $6.3 \mu\text{m}$ and CH_4 at $7.7 \mu\text{m}$ for a cloud free and Earth-analogue cloud coverage model. The left panel of each row shows the relative flux as planet-to-star contrast ratio, the middle and right panel show the specific, top-of-atmosphere flux for a clear and 60% cloud coverage

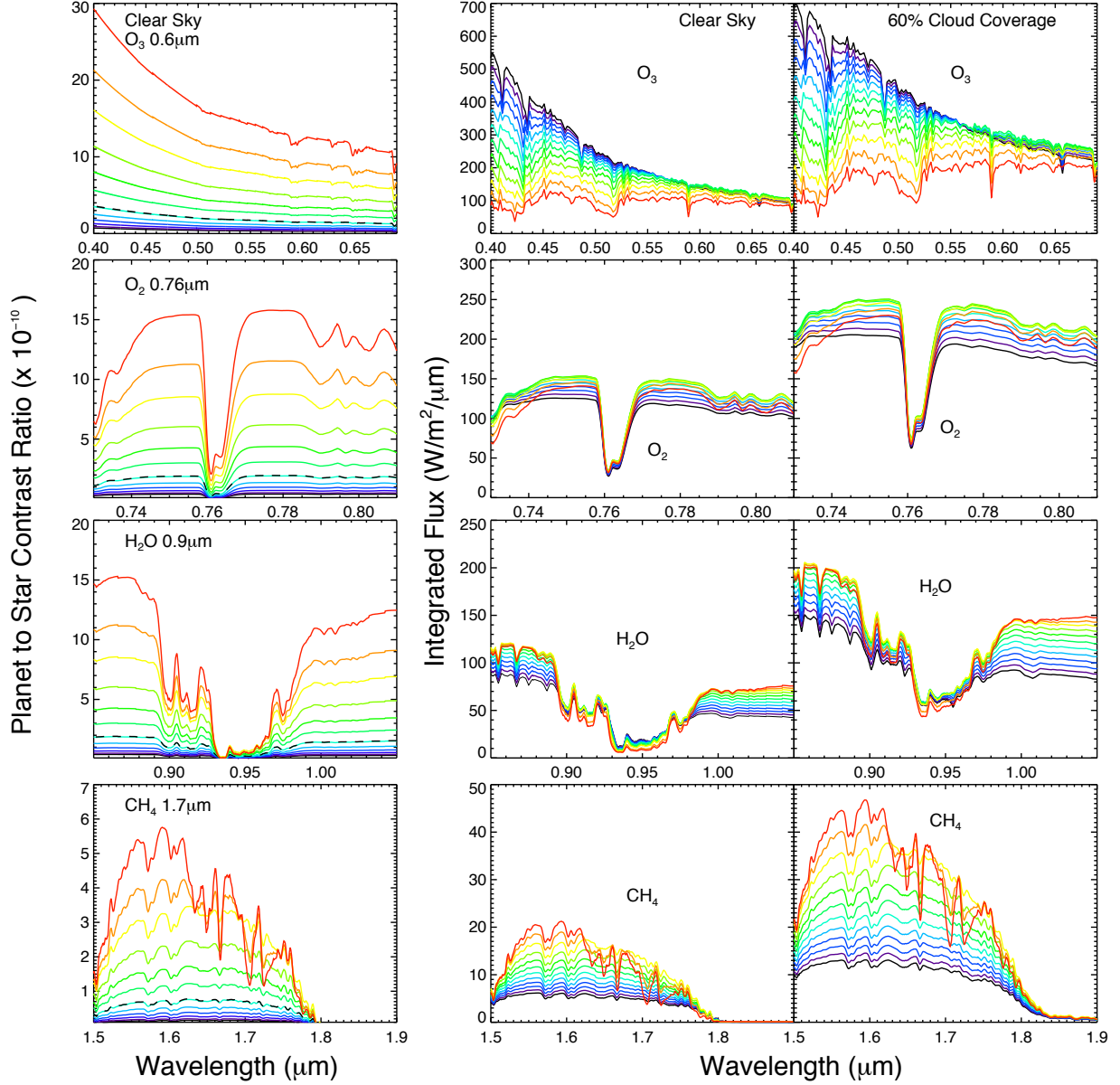


Fig. 9.— Individual features of O_3 at $0.6 \mu\text{m}$, O_2 and $0.76 \mu\text{m}$, H_2O at $0.95 \mu\text{m}$, and CH_4 at $1.7 \mu\text{m}$ for F0V – K7V grid stars (left) planet-to-star contrast ratio and absolute flux levels (middle) for a clear sky and (right) 60% cloud coverage model. Note the different y-axes. Legend and color coding are the same in figures 6 to 11.

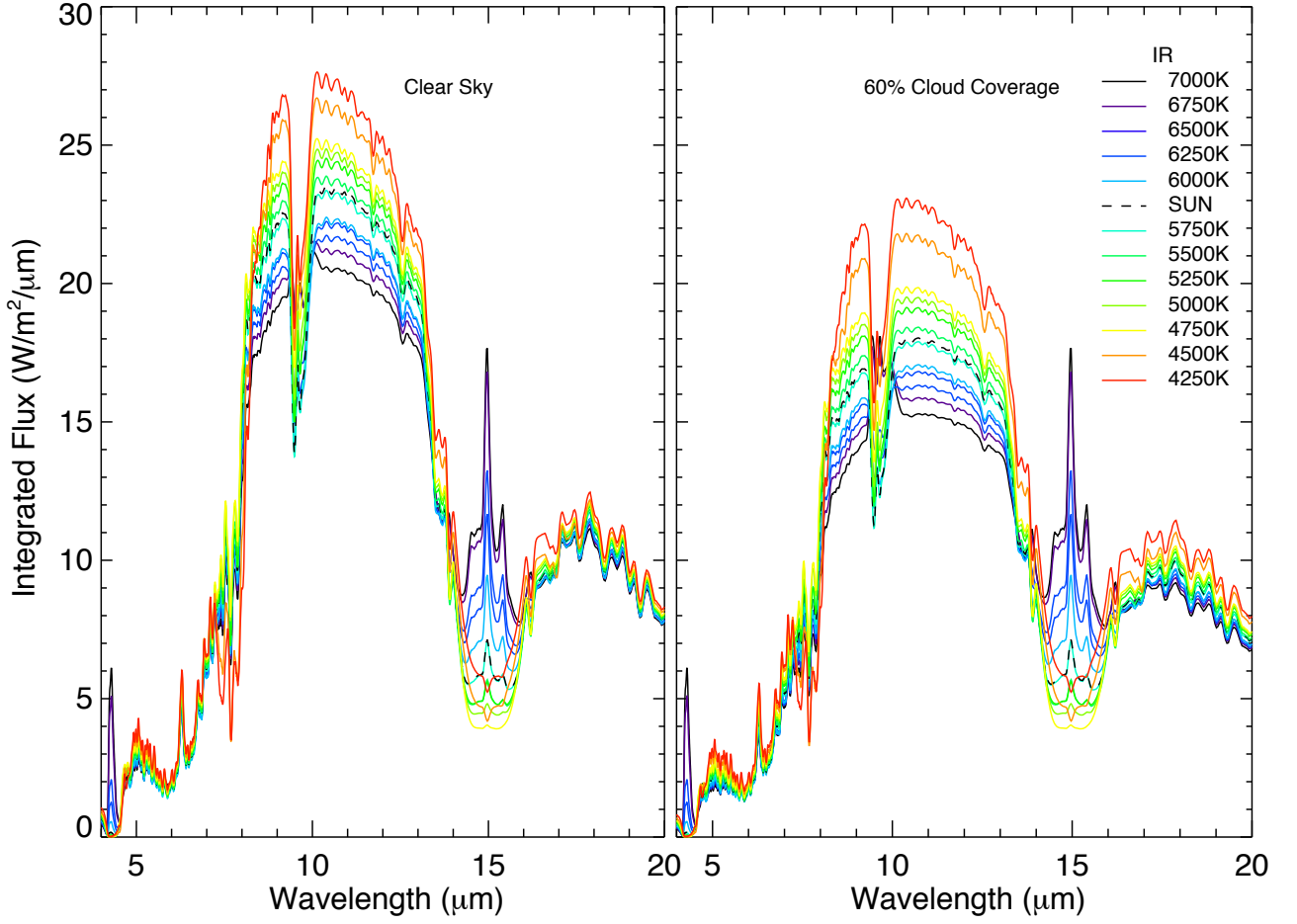


Fig. 10.— Smoothed, disk-integrated IR spectra at the top of the atmosphere (TOA) for Earth-like planets around F0V to K7V grid stars for both a clear sky (left) and 60% cloud coverage (right) model.

case, respectively.

In the clear sky model, the depth of the O_3 feature at $9.6\mu\text{m}$ decreases for planet models orbiting hot grid stars, despite increasing O_3 abundance, due to lower contrast between the continuum and absorption layer temperature. For Earth-analogue cloud cover, however, O_3 is seen in emission for $T_{\text{eff}} > 6500\text{K}$ due to the lower continuum temperature.

Due to the hot stratosphere for all grid stars with $T_{\text{eff}} > 6000\text{K}$, the CO_2 absorption

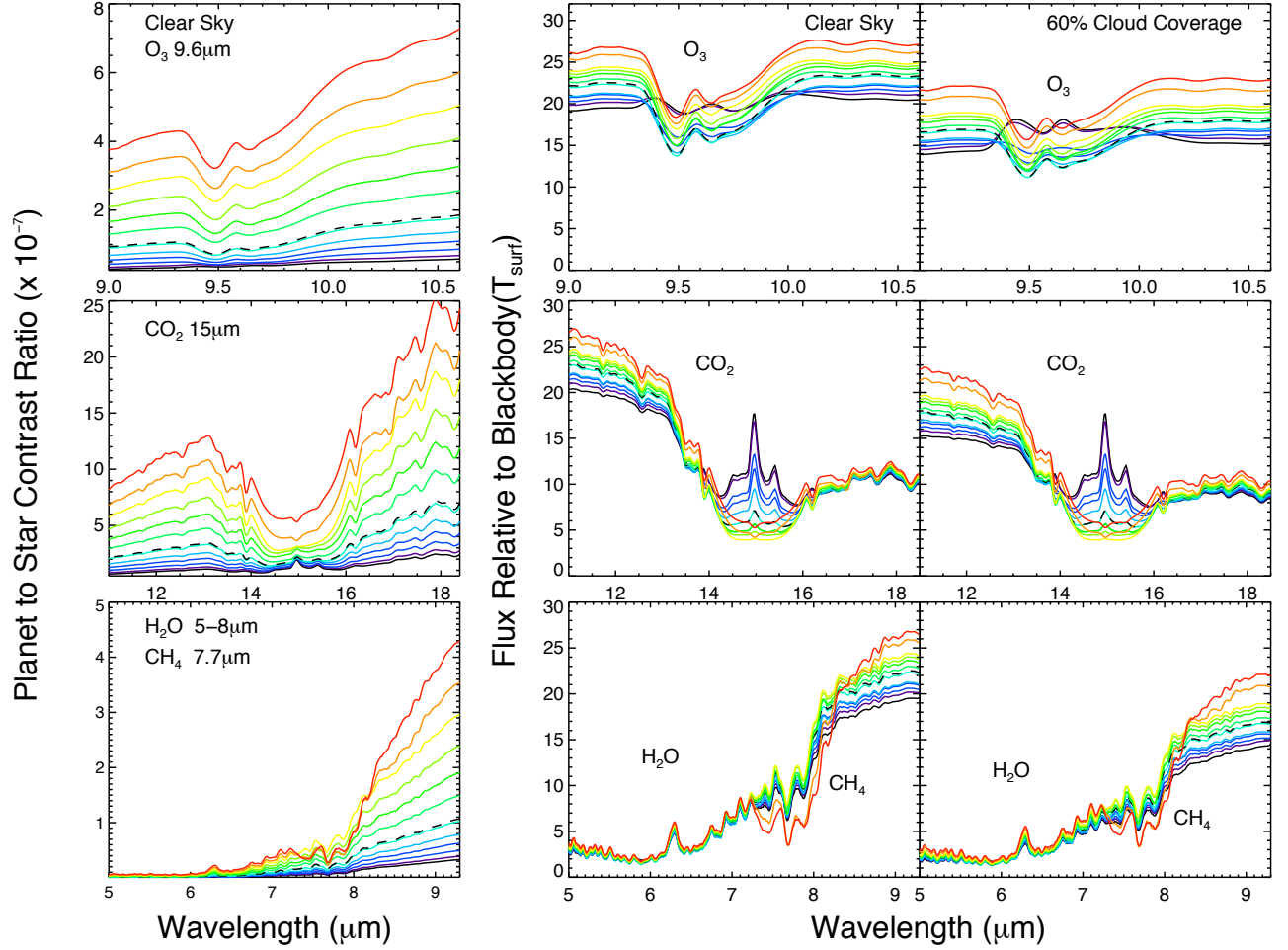


Fig. 11.— Individual features of O_3 at $9.6 \mu\text{m}$, CO_2 and $15 \mu\text{m}$, H_2O at $5\text{--}8 \mu\text{m}$, and CH_4 at $7.7 \mu\text{m}$ for F0V – K7V grid stars (left) planet-to-star contrast ratio and absolute flux levels (middle) for a clear sky and (right) 60% cloud coverage model. Legend and color coding are the same in figures 2 to 8.

feature at $15 \mu\text{m}$ has a prominent central emission peak. Clouds reduce the continuum level and the depth of the observable CO_2 feature.

The CH_4 feature at $7.7 \mu\text{m}$ is prominent in the planetary spectra around cool grid stars due to high CH_4 abundance in low UV environments. The CH_4 feature is also partially

obscured by the wings of the H_2O feature at $5\text{--}8\mu\text{m}$. The depth of the H_2O features at $5\text{--}8\mu\text{m}$ and $18+\mu\text{m}$ do not change significantly even though H_2O abundance increases for cool grid stars. Clouds reduce the continuum level and the depth of the observable H_2O features.

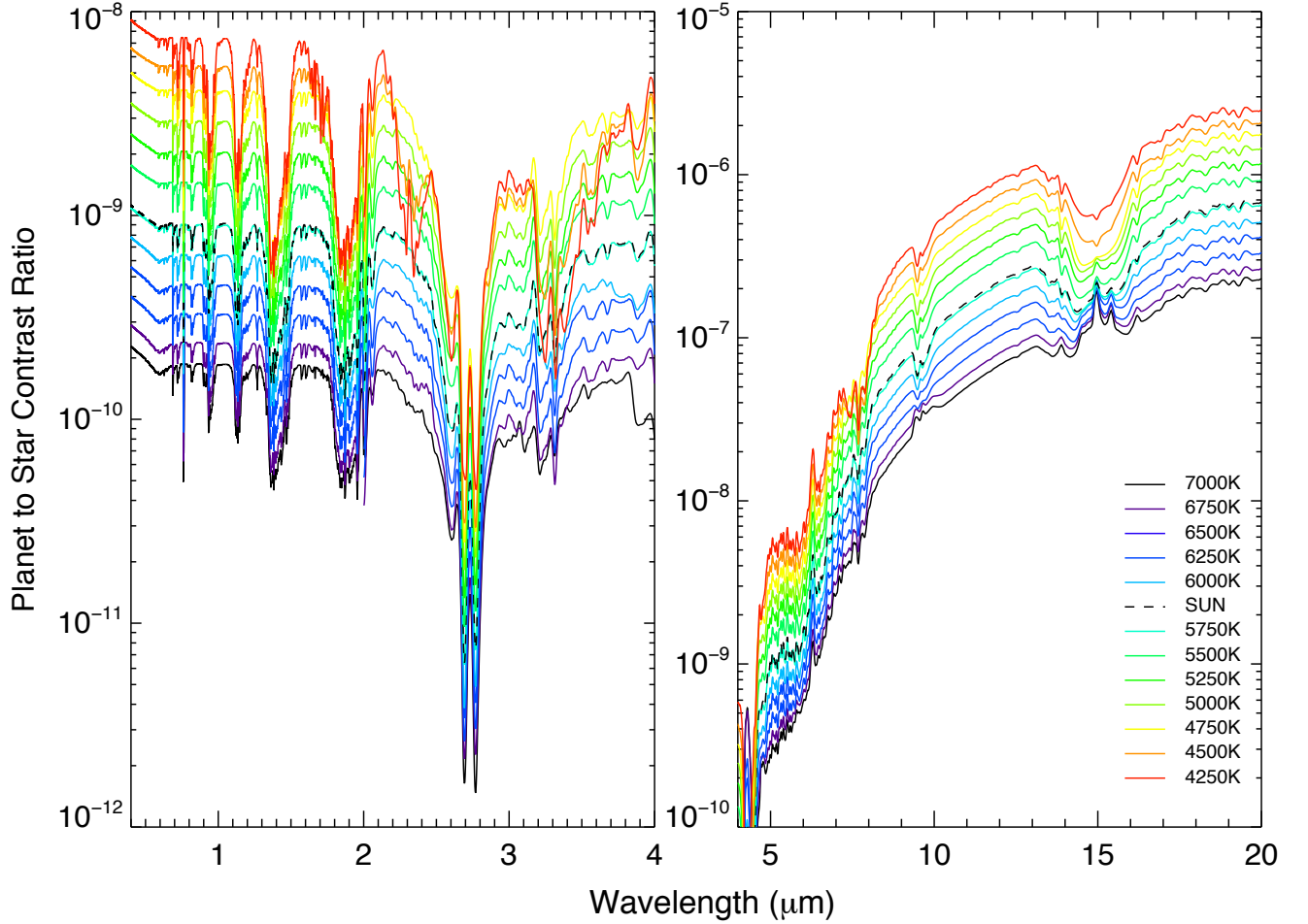


Fig. 12.— Contrast Ratio of Earth-like planets for Earth-analogue cloud coverage.

Fig. 12 shows planet-to-star contrast ratio for Earth-analog cloud cover of an Earth-like planet from which the photometric precision required can be calculated. The planet-to-star contrast ratio is between 10^{-8} to 10^{-11} in the VIS/NIR and between about 10^{-6} and 10^{-10} in the IR for the grid stars. For the whole wavelength range, the contrast ratio improves for cool grid stars.

4.3. The effect of clouds on an Earth-like planet spectra from 0.4 - 20 μ m

Fig. 13 shows Earth-like planet spectra for 100% cloud cover at 1km, 6km and 12km from 0.4 to 20 μ m for three sample grid stars with $T_{\text{eff}} = 7000\text{K}$ (top), 5750K (middle), and 4250K (bottom). The clear sky spectrum is shown as dashed line for comparison. Clouds increase the reflectivity of an Earth-like planet in the VIS to NIR substantially and therefore overall increase the equivalent width of all observable features, even though they block access to some of the lower atmosphere. Clouds decrease the overall emitted flux of an Earth-like planet in the IR slightly because they radiate at lower temperatures and therefore overall decrease the equivalent width of all observable absorption features, even though they can increase the relative depth of a spectral feature due to lowering the continuum temperature of the planet.

Fig. 14 shows the individual chemical absorption features as discussed in section 4.1 and 4.2 on a relative scale for H₂O, CO₂, O₂, O₃, CH₄, N₂O and CH₃Cl from 0.4 μ m to 20 μ m to complement the spectra shown in Figs. 5-9, that focus on the remote detectability of individual features for future space missions.

5. DISCUSSION

When choosing IUE stars to for our stellar spectral grid, we avoided stars of unusual variability, but did not exclude stars that had representative variability of its stellar class. Several of our representative K stars are variables of the BY Draconis type which is a common variable in this stellar type. We preferentially choose stars with near solar metallicity when possible; however, the IUE database does not provide candidate stars at each temperature of solar metallicity. Several stars have lower than solar metallicity. We compared a subsolar stellar metallicity with a solar metallicity spectra model and found

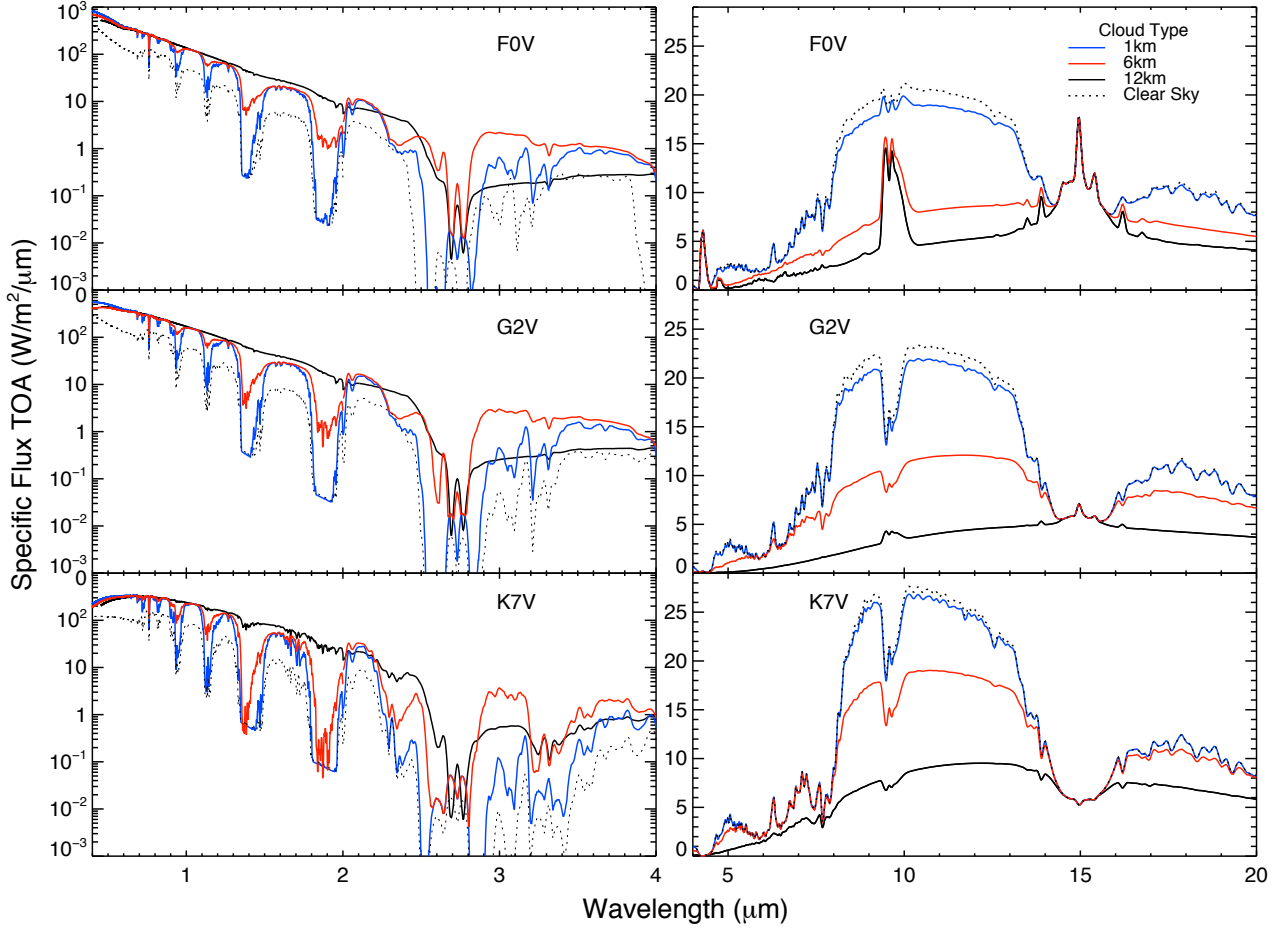


Fig. 13.— Spectra of Earth-like planets for 100% cloud coverage at 3 cloud heights (1km, 6km and 12km, blue, red and black line, respectively) as well as clear sky spectrum (dashed line) from 0.4 to 20 μm , orbiting a $T_{\text{eff}} = 7000\text{K}$ (top) $T_{\text{eff}} = 5750\text{K}$ (middle), and $T_{\text{eff}} = 4250\text{K}$ (bottom) grid star for comparison.

that the difference does not impact our results.

Observability of Biosignatures: Detecting the combination of O_2 or O_3 and CH_4 for emergent spectra and secondary eclipse measurements requires observations in the IR or in the VIS/NIR up to 3 μm to include the 2.4 μm CH_4 feature in that spectral range. The strength of the absorption features depend on the stellar effective temperature of the

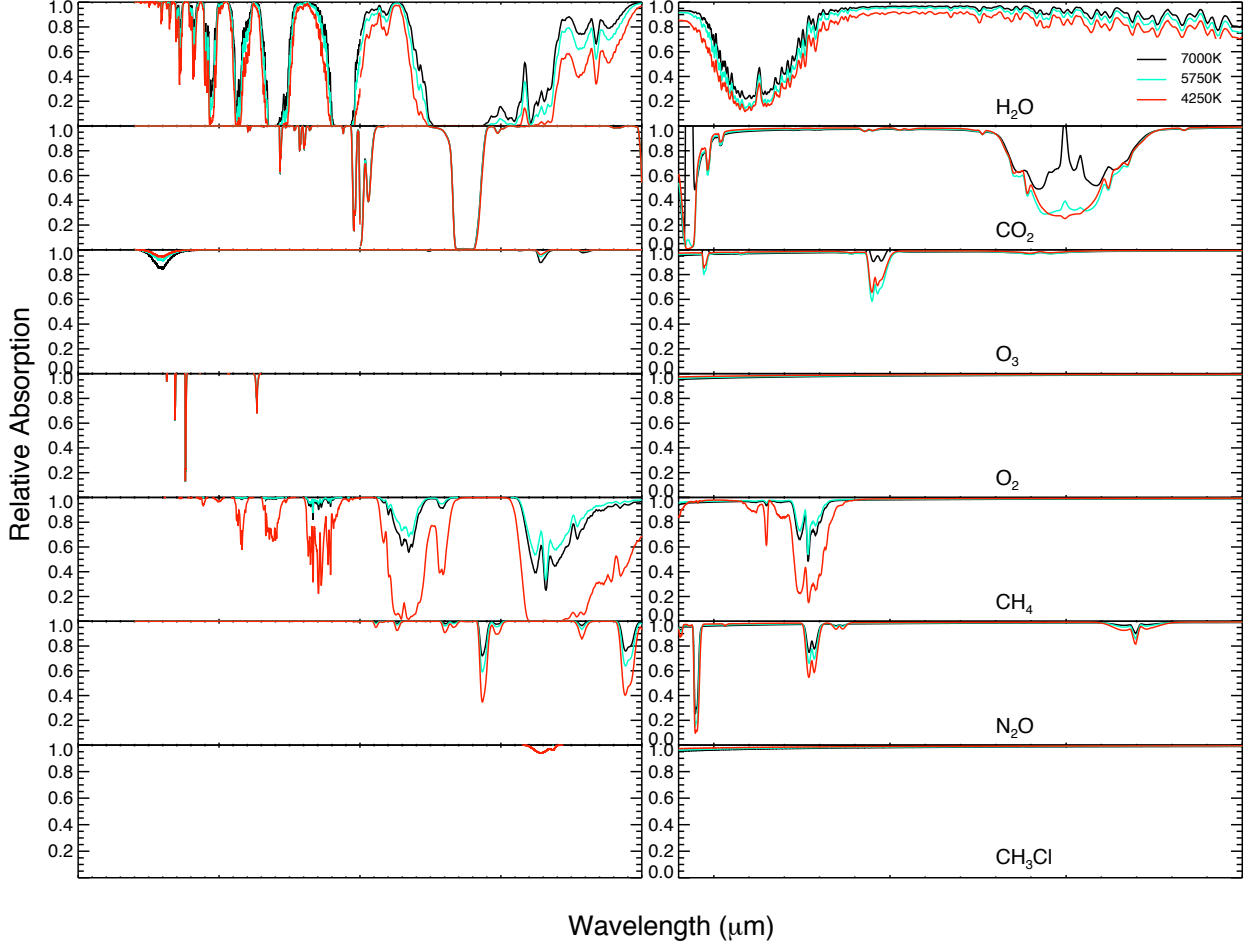


Fig. 14.— Relative absorption of individual chemical species H_2O , CO_2 , O_2 , O_3 , CH_4 , N_2O and CH_3Cl for three sample grid stars with $T_{\text{eff}} = 7000\text{K}$, 5750K , and 4250K .

host star and vary significantly between stellar types. In the IR, CH_4 at $7.7 \mu\text{m}$ is more detectable at low resolution for cool grid stars than hot grid stars. The $9.6 \mu\text{m}$ O_3 feature is deepest for mid to cool stars and becomes less detectable for hotter stars. However around our hottest grid stars, the $9.6 \mu\text{m}$ O_3 feature becomes an apparent emission feature for cloudy atmospheres. The narrow O_2 feature in the VIS at $0.72 \mu\text{m}$ is of comparable strength for all grid stars. H_2O has strong features for all grid stars over the whole wavelength range.

N_2O and CH_3Cl have features from the NIR to IR (see Fig. 14) but in modern Earth

concentrations do not have a strong enough feature to be detected with low resolution. For the clear sky models, the vegetation red edge is detectable due to the order of magnitude increased reflectance from $0.7\ \mu\text{m}$ to $0.75\ \mu\text{m}$ for all grid stars. Clouds obscure that feature (see Fig. 8).

For detecting an oxidizing gas in combination with a reducing gas in Earth-like planet atmosphere models, the coolest grid stars in our sample are the best targets. In this paper we have not modeled planets orbiting stars cooler than 4000K to provide a consistent set of planetary models. As discussed in Segura et al. 2005, cool host stars with low UV flux, provide an environment that leads to run-away CH_4 accumulation in the atmosphere and therefore the model for Earth-like planets around M-dwarfs often use abiotic CH_4 levels, not consistent with Earth-analogue models used in this study. We will explore this effect in a future work.

No noise has been added to these model spectra to provide input models for a wide variety of instrument simulators for both secondary eclipse and direct detection simulations. Different instrument simulators for JWST (see e.g. Deming et al. 2009; Kaltenegger & Traub 2009) explore the capability of JWST’s MIRI and NIRSpec Instrument to characterize extrasolar planets down to Earth-like planets, with interesting results for planets around close-by as well as luminous host stars. Several new results are forthcoming by several groups that will provide realistic instrument parameters that can be used to determine detectability of these absorption features. Future ground and space based telescopes are being designed to characterize exoplanets down to Earth-like planets and will provide interesting opportunities to observe atmospheric features, especially for Super-Earths, with radii up to 2 times Earth’s radius and therefore 4 times the flux and planet-to-star contrast ratio levels quoted for Earth-size planets shown in Figs. 8-14.

In addition to the size of the planet, future observations will occur at different positions

throughout the planet’s orbit. The maximum observable planetary flux in the visible scales with the illuminated fraction of the planet, that is “visible” to the observer. In the IR the maximum flux remains constant throughout the planet’s orbit, assuming a similar temperature on the day and night side. In Fig. 15 we show the absolute specific flux levels at full phase, gibbous phase, and quadrature scaled with a Lambert phase function (phase angles of 0° , 45° , and 90° , respectively) for 60% cloud coverage Earth-like planets orbiting three grid stars with $T_{\text{eff}} = 7000\text{K}$, 5750K and 4250K to show the effect of orbital position (see also Robinson et al., 2011). We scaled our full-phase simulations to other phases using a Lambert phase function. For quadrature, representing an average viewing geometry, the contrast ratios presented in Fig. 13 will be a factor of 2 lower in the visible. Assuming the planet has efficient heat transport from the day to night side, the specific flux levels and contrast ratios in the IR will be unchanged.

6. CONCLUSIONS

We calculated the spectra for terrestrial atmosphere models receiving the same incoming flux as Earth when orbiting a grid of host stars with $T_{\text{eff}} = 4250\text{K}$ to $T_{\text{eff}} = 7000\text{K}$ in 250K increments, comprehensively covering the full FGK stellar range. We discuss the spectral features for clear and cloudy atmosphere models and compare the effect of the stars SED and UV flux on both the atmospheric composition as well as the detectable atmospheric features in section 3 and 4.

Increasing UV environments (generally coupled with increasing stellar T_{eff} for main sequence stars) result in: increasing concentration of O_3 from photolysis, increasing stratospheric H_2O from O_3 shielding, increasing OH based on increased O_3 and H_2O concentrations, and decreasing CH_4 , CH_3Cl , and N_2O from photolysis and reactions with OH. Increasing stellar temperatures and corresponding decreasing planetary surface

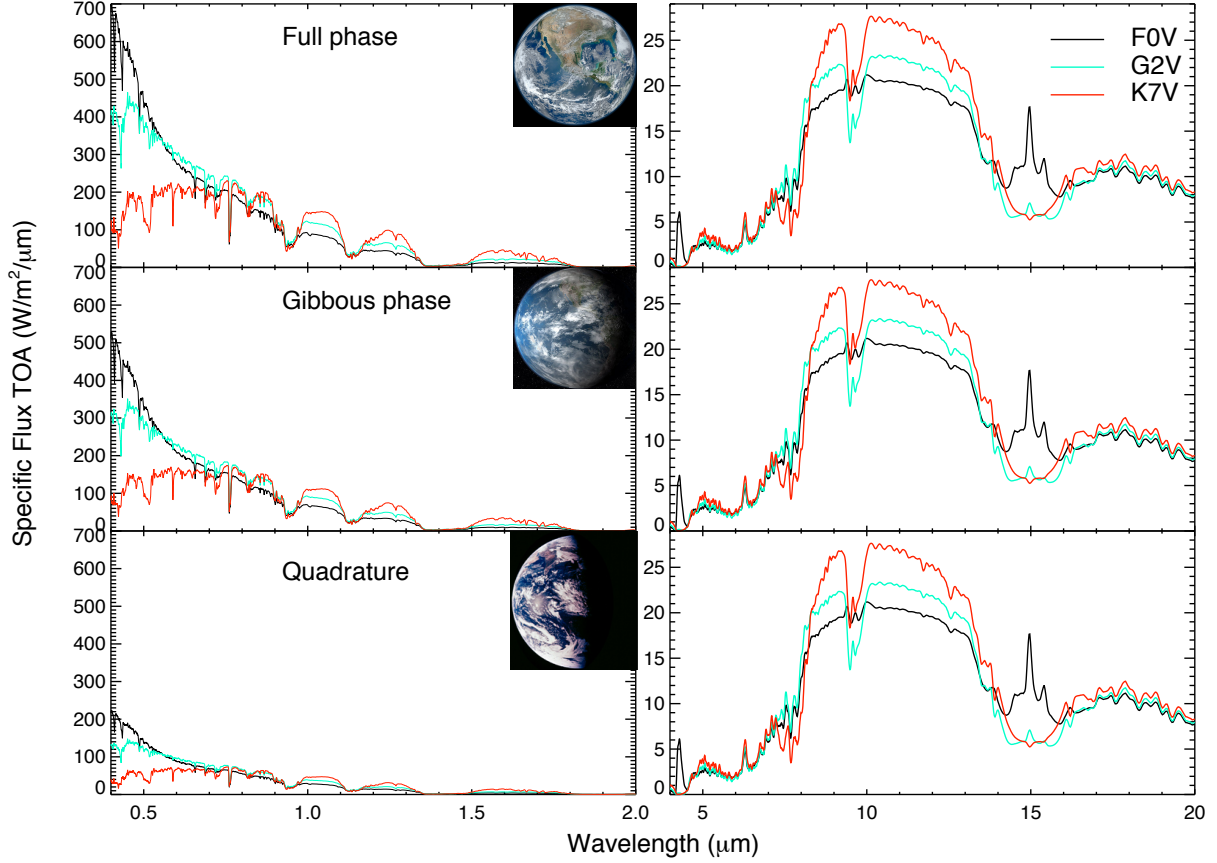


Fig. 15.— Absolute specific flux values for clear-sky Earth-like planets around three different grid stars with $T_{\text{eff}} = 7000\text{K}$, 5750K , and 4250K in the visible and IR for 3 phases: full phase, gibbous phase, and quadrature with corresponding phase angles of 0, 45, and 90, respectively.

temperatures result in: decreasing tropospheric H_2O due to decreased temperatures, decreasing stratospheric H_2O from transport, and decreasing reaction rates of OH with CH_4 , N_2O and CH_3Cl . The overall effect as the stellar effective temperature of the main sequence grid stars increases, is an increase in O_3 and OH concentration, a decrease in tropospheric H_2O (but an increase stratospheric H_2O), and a decrease in stratospheric CH_4 , N_2O , CH_3Cl .

In the infrared, the temperature contrast between the surface and the continuum layer

is strongly impacts the depth of spectral features. While O_3 increases for hotter main sequence stars the strength of the $9.6\mu\text{m}$ band decreases due to the decrease temperature difference between the continuum and the emitting layer. For hot stars, with $T_{\text{eff}} > 6750\text{K}$ the O_3 feature appears as emission due to the contrast to the continuum.

Our results provides a grid of atmospheric compositions as well as model spectra from the VIS to the IR for JWST and other future direct detection mission design concepts. The model spectra in this paper are available at www.cfa.harvard.edu/~srugheimer/FGKspectra/.

L.K. acknowledge support from DFG funding ENP Ka 3142/1-1 and NAI. This research has made use of the NASA/IPAC/NEExScI Star and Exoplanet Database, which is operated by the Jet Propulsion Laboratory, California Institute of Technology, under contract with the National Aeronautics and Space Administration.

The UV data presented in this paper were obtained from the Multimission Archive at the Space Telescope Science Institute (MAST). STScI is operated by the Association of Universities for Research in Astronomy, Inc., under NASA contract NAS5-26555. Support for MAST for non-HST data is provided by the NASA Office of Space Science via grant NAG5-7584 and by other grants and contracts.

REFERENCES

- Batalha, N. M., Rowe, J. F., Bryson, S. T., et al. 2013, *ApJS*, 204, 24
- Beichman, C., Lawson, P., Lay, O., et al. 2006, in *Society of Photo-Optical Instrumentation Engineers (SPIE) Conference Series*, Vol. 6268, *Society of Photo-Optical Instrumentation Engineers (SPIE) Conference Series*
- Beichman, C. A., Woolf, N. J., & Lindensmith, C. A. 1999, *The Terrestrial Planet Finder (TPF) : a NASA Origins Program to search for habitable planets (Pasadena, CA: JPL Publications)*
- Borucki, W. J., Koch, D. G., Basri, G., et al. 2011, *ApJ*, 736, 19
- Cash, W. 2006, *Nature*, 442, 51
- Cayrel de Strobel, G., Soubiran, C., Friel, E., Ralite, N., & Francois, P. 1997, *Astronomy and Astrophysics Supplement Series*, 124, 299
- de Strobel, G. C., Soubiran, C., & Ralite, N. 2001, *arXiv preprint astro-ph/0106438*
- Deming, D., Seager, S., Winn, J., et al. 2009, *PASP*, 121, 952
- Des Marais, D. J., Harwit, M. O., Jucks, K. W., et al. 2002, *Astrobiology*, 2, 153
- Di Folco, E., Thévenin, F., Kervella, P., et al. 2004, *Astronomy and Astrophysics*, 426, 601
- Flower, P. J. 1996, *The Astrophysical Journal*, 469, 355
- Forster, P., Ramaswamy, V., Artaxo, P., et al. 2007, in *Climate Change 2007: The Physical Science Basis. Contribution of Working Group I to the Fourth Assessment Report of the Intergovernmental Panel on Climate Change*, ed. S. Solomon, D. Qin, M. Manning, Z. Chen, M. Marquis, K. B. Averyt, M. Tignor, & H. L. Miller

- (Cambridge University Press, Cambridge, United Kingdom and New York, NY, USA.)
- Gardner, J. P., Mather, J. C., Clampin, M., et al. 2006, *Space Sci. Rev.*, 123, 485
- Gray, D. 1992, *The Observation and Analysis of Stellar Photospheres* (The Observation and Analysis of Stellar Photospheres, by David F. Gray, pp. 470. ISBN 0521408687. Cambridge, UK (Cambridge University Press), 431
- Grenfell, J. L., Stracke, B., von Paris, P., et al. 2007, *Planetary and Space Science*, 55, 661
- Haqq-Misra, J. D., Domagal-Goldman, S. D., Kasting, P. J., & Kasting, J. F. 2008, *Astrobiology*, 8, 1127
- Kaltenegger, L. 2010, *ApJL*, 712, L125
- Kaltenegger, L., Henning, W. G., & Sasselov, D. D. 2010, *AJ*, 140, 1370
- Kaltenegger, L., & Sasselov, D. 2010, *ApJ*, 708, 1162
- . 2011, *ApJL*, 736, L25
- Kaltenegger, L., & Traub, W. A. 2009, *ApJ*, 698, 519
- Kaltenegger, L., Traub, W. A., & Jucks, K. W. 2007, *ApJ*, 658, 598
- Kasting, J. F., & Ackerman, T. P. 1986, *Science*, 234, 1383
- Kasting, J. F., Holland, H. D., & Pinto, J. P. 1985, *J. Geophys. Res.*, 90, 10497
- Kasting, J. F., Pollack, J. B., & Crisp, D. 1984, *J. Atmos. Chem.*, 1
- Kitzmann, D., Patzer, A. B. C., von Paris, P., Godolt, M., & Rauer, H. 2011a, *A&A*, 531, A62

—. 2011b, *A&A*, 534, A63

Klaasen, K. P., A’Hearn, M. F., Baca, M., et al. 2008, *Review of Scientific Instruments*, 79, 091301

Kurucz, R. L. 1979, *The Astrophysical Journal Supplement Series*, 40, 1

Livengood, T. A., Deming, L. D., A’Hearn, M. F., et al. 2011, *Astrobiology*, 11, 907

Lovelock, J. E. 1975, *Royal Society of London Proceedings Series B*, 189, 167

Massa, D., & Fitzpatrick, E. L. 1998, arXiv preprint astro-ph/9812152

—. 2000, *The Astrophysical Journal Supplement Series*, 126, 517

Meadows, V. S. 2005, *Proceedings of the International Astronomical Union*, 1, 25

Pallé, E., Ford, E. B., Seager, S., Montañés-Rodríguez, P., & Vazquez, M. 2008, *The Astrophysical Journal*, 676, 1319

Pavlov, A. A., Hurtgen, M. T., Kasting, J. F., & Arthur, M. A. 2003, *Geology*, 31, 87

Pavlov, A. A., & Kasting, J. F. 2002, *Astrobiology*, 2, 27

Pavlov, A. A., Kasting, J. F., Brown, L. L., Rages, K. A., & Freedman, R. 2000, *J. Geophys. Res.*, 105, 11981

Robinson, T. D., Meadows, V. S., Crisp, D., et al. 2011, *Astrobiology*, 11, 393

Sagan, C., Thompson, W. R., Carlson, R., Gurnett, D., & Hord, C. 1993, *Nature*, 365, 715

Schindler, T. L., & Kasting, J. F. 2000, *Icarus*, 145, 262

Seager, S., Turner, E. L., Schafer, J., & Ford, E. B. 2005, *Astrobiology*, 5, 372

Segura, A., Kasting, J. F., Meadows, V., et al. 2005, *Astrobiology*, 5, 706

- Segura, A., Krellove, K., Kasting, J. F., et al. 2003, *Astrobiology*, 3, 689
- Segura, A., Meadows, V. S., Kasting, J. F., Crisp, D., & Cohen, M. 2007, *A&A*, 472, 665
- Segura, A., Walkowicz, L. M., Meadows, V., Kasting, J., & Hawley, S. 2010, *Astrobiology*, 10, 751
- Selsis, F. 2000, in *ESA Special Publication*, Vol. 451, *Darwin and Astronomy : the Infrared Space Interferometer*, ed. B. Schürmann, 133
- Sneep, M., & Ubachs, W. 2005, *Journal of Quantitative Spectroscopy and Radiative Transfer*, 92, 293
- Toon, O. B., McKay, C. P., Ackerman, T. P., & Santhanam, K. 1989, *J. Geophys. Res.*, 94, 16287
- Traub, W. A., & Stier, M. T. 1976, *Appl. Opt.*, 15, 364
- Traub, W. A., Levine, M., Shaklan, S., et al. 2006, in *Society of Photo-Optical Instrumentation Engineers (SPIE) Conference Series*, Vol. 6268, *Society of Photo-Optical Instrumentation Engineers (SPIE) Conference Series*
- Udry, S., Bonfils, X., Delfosse, X., et al. 2007, *A&A*, 469, L43
- Valenti, J. A., & Fischer, D. A. 2005, *The Astrophysical Journal Supplement Series*, 159, 141